Toward a Stochastic Relaxation for the Quasi-Equilibrium Theory of Cumulus Parameterization: Multicloud Instability, Multiple Equilibria, and Chaotic Dynamics

Boualem Khouider & Etienne Leclerc

July 2019

JAMES | Journal of Advances in Modeling Earth Systems

AGU100 ADVANCING EARTH AND SPACE SCIENCE

Check for updates

RESEARCH ARTICLE
10.1029/2019MS001627

Key Points:
- The prognostic closure equations for cumulus parameterization are unstable when cloud-cloud interactions were included
- The cloud work function-cloud base mass flux equations are coupled to new equations for the cloud area fractions
- The three-way coupled equations exhibit multiple equilibria, limit cycles, and chaotic behavior, mimicking organized convection

Correspondence to:
Boualem Khouider,
khouider@uvic.ca

Citation:
Khouider B., & Leclerc, E. (2019). Toward a stochastic relaxation for the quasi-equilibrium theory of cumulus parameterization: Multicloud instability, multiple equilibria, and chaotic dynamics. *Journal of Advances in Modeling Earth Systems*, *11*, 2474–2502. https://doi.org/10.1029/2019MS001627

Received 22 JAN 2019
Accepted 8 JUL 2019
Accepted article online 17 JUL 2019
Published online 5 AUG 2019

Toward a Stochastic Relaxation for the Quasi-Equilibrium Theory of Cumulus Parameterization: Multicloud Instability, Multiple Equilibria, and Chaotic Dynamics

Boualem Khouider[1] and Etienne Leclerc[1]

[1] Department of Mathematics and Statistics, University of Victoria, Victoria, British Columbia, Canada

Abstract The representation of clouds and organized tropical convection remains one of the biggest sources of uncertainties in climate and long-term weather prediction models. Some of the most common cumulus parameterization schemes, namely, mass-flux schemes, rely on the quasi-equilibrium (QE) closure, which assumes that convection consumes the large-scale instability and restores large-scale equilibrium instantaneously. However, the QE hypothesis has been challenged both conceptually and in practice. Subsequently, the QE assumption was relaxed, and instead, prognostic equations for the cloud work function (CWF) and the cumulus kinetic energy (CKE) were derived and used. It was shown that even if the CWF kernel serves to damp the CWF, the prognostic system exhibits damped oscillations on a timescale of a few hours, giving parameterized-cumulus-clouds enough memory to interact with each other, with the environment, and with stratiform anvils in particular. Herein, we show that when cloud-cloud interactions are reintroduced into the CWF-CKE equations, the coupled system becomes unstable. Moreover, we couple the CWF-CKE prognostic equations to dynamical equations for the cloud area fractions, based on the mean field limit of a stochastic multicloud model. Qualitative analysis and numerical simulations show that the CKE-CWF-cloud area fraction equations exhibit interesting dynamics including multiple equilibria, limit cycles, and chaotic behavior both when the large-scale forcing is held fixed and when it oscillates with various frequencies. This is representative of cumulus convection variability, and its capability to transition between various regimes of organization at multiple scales and regimes of scattered convection, in an intermittent and chaotic fashion.

1. Introduction

Climate and long-term numerical weather prediction (NWP) models are large computer codes that approximate the equations of atmosphere and ocean flow motions, among other components of the Earth system, on coarse meshes ranging from 10 km to up to 200 km in the horizontal. On such coarse resolutions, many physical phenomena that are of central importance for the climate and weather systems appear as subgrid processes that are represented by ad hoc/empirical recipes and complex mathematical models known as parameterizations. Radiative processes, boundary layer turbulence, gravity wave drag, vegetation, air-sea interaction, clouds, and precipitations are only a few examples of physical phenomena that are exclusively parameterized in a typical climate or long-term numerical weather prediction model (Emanuel & Raymond, 1993; Stensrud, 2007). The representation of cumulus convection has in particular evolved, over the span of less than 20 years, from very simplistic ideas such as the wave convective instability of the second kind of Charney and Eliassen (1964) and Kuo (1965) and the convective adjustment process of Manabe et al. (1965) to the more sophisticated so-called mass flux framework introduced by Arakawa and Schubert (1974).

In wave convective instability of the second kind models, which are also known as moisture-convergence -closure-type schemes (Kuo, 1974), the large-scale convergence of moisture is assumed to directly drive convection while in the adjustment schemes, convection assumes the task of always bringing the large-scale state back to a moist-dynamical equilibrium (Betts, 1986; Betts & Miller, 1986). In mass-flux schemes, the vertical transport of mass, heat, and water substances by updrafts and downdrafts is systematically represented, and a closure is sought in terms of energy and mass balances. Due to its near-realistic representation of the process of convection, the mass-flux idea has led to many refinements and simplifications that have been implemented in several (if not the majority) of existing climate and weather prediction models

(Ganai et al., 2016; Kain & Fritsch, 1990; Moorthi & Suarez, 1992; Tiedtke, 1993; Zhang & McFarlane, 1995). Although the results are not satisfactory, not much progress has been made in this area until the advent of the idea of superparameterization. This led some scientists to call for “breaking the convection parameterization deadlock” (Randall et al., 2003). In superparameterization, a two-dimensional cloud resolving model is embedded within each climate model grid box in lieu of a convective parameterization (Grabowski, 2004; Khairoutdinov et al., 2005).

Typically, mass flux cumulus schemes assume an arbitrary spectrum of cloud types or convective plumes each of which is identified by its entrainment rate λ and an associated detrainment level $z_D(\lambda)$ (Arakawa & Schubert, 1974). The updraft and downdraft mass fluxes associated with each ensemble of cloud types can then be calculated by integrating the dynamical equations of the convecting fluid while taking into account the hydrological cycle and the thermodynamics of phase change. Under the top-hat approximation assumption, a single updraft value and a single downdraft value for the vertical momentum (mass flux) and moist-thermodynamic variables (such as temperature, water vapor, and liquid water mixing ratios) are used at each vertical level. The bulk mass flux, bulk entrainment, and bulk detrainment rates are then calculated and used directly to estimate the “unresolved” convective-turbulent-like fluxes together with the bulk heating/cooling and drying/moistening rates for the large scale-resolved dynamics (Zhang & McFarlane, 1995). However, as in turbulence modeling, a closure problem arises mainly because the convective mass flux requires the knowledge of both the vertical velocity and the area fraction occupied by the updraft and downdraft ensembles, while only one equation can be systematically derived from mass and energy balance. Instead, a closure for the mass flux at cloud base is required. Arakawa and Schubert (1974) have thus introduced the idea of quasi-equilibrium (QE) where the convection is assumed to consume the instability, represented by a cloud work function (CWF), as soon as it is created by the large-scale dynamics. This leads to the inversion of a nonlinear steady state equation for the bulk updraft mass flux at cloud base, associated with each cloud type subensemble. The QE assumption is theoretically and empirically justified to some extent when the grid mesh is coarse enough to contain a large enough ensemble of clouds and so that the total cloud area fraction (CAF) is small enough (Arakawa & Schubert, 1974; Lord & Arakawa, 1980).

Despite sustained efforts throughout the last few decades (Arakawa, 2004; Kim & Kang, 2012; Mapes & Neale, 2011), the representation of clouds and organized tropical convection is still one of the biggest sources of uncertainties in current and previous generation models (Meehl et al., 2007). The convective parametrization schemes have been blamed for the observed biases in the predicted amounts of rainfall and major weather patterns, especially in the tropics (Hung et al., 2013; Jiang et al., 2015; Kim et al., 2009; Lin et al., 2008; Slingo et al., 1996). Among other issues, the QE assumption has been pointed out as being the Achilles' heel of mass flux parameterizations, as it is incapable of representing the subgrid variability associated with organized tropical convection, for example. Organized convection in the tropics involves a hierarchy of multiple temporal and spatial scales, ranging from the convective cell of 1 to 10 km and a few hours, to mesoscale cloud clusters and superclusters ranging from hundreds to a few thousand kilometers and a few days, to their envelopes evolving on the intraseasonal and planetary scales (Khouider et al., 2013; Moncrieff & Klinker, 1997; Lin et al., 2006; Majda, 2007; Moncrieff, 1992).

The criticism of the QE equilibrium theory increased widely when high-resolution weather prediction models failed to provide adequate forecasts and when the modeling community stumbled into the dilemma of the gray-zone resolutions where grid sizes are around 10 km. Such intermediate resolutions are believed to be too small for the QE's large cloud ensemble assumption to be valid and too large to resolve actual clouds (Buizza et al., 1999; Grell & Devenyi, 2002; Sun et al., 2014). New ideas on how to account for the change in resolution started to emerge, such as the introduction of the notion of scale-aware parameterizations (e.g., Arakawa & Wu, 2013;Grell & Freitas, 2014).

Among the suggested remedies, Pan and Randall (1998) came up with the idea of relaxing the QE assumption for the Arakawa and Schubert parameterization by prognostic equations. They systematically use the cumulus kinetic energy (CKE) equation and replace the QE closure by a relation between CKE and the cloud base mass flux as it is done in boundary layer convection schemes (Bretherton & Park, 2008). They assume that the CKE is proportional to the square of the cloud base mass flux with a fixed proportionality parameter α depending only on the cloud type's vertical profile. The cloud base mass flux is coupled to the evolution equation of the CWF so that the convection instability is continuously consumed as it is converted to CKE. Pan and Randall thus use a prognostic equation for the CKE associated with each cloud type in lieu of the QE assumption to allow the convective parameterization to have some memory while integrated within the climate model. This procedure amounts to forgoing the scale separation assumption between cumulus convection and large-scale dynamics, though some similarity between the QE adjustment time and the parameter α has been suggested.

A more radical alternative to breaking the QE assumption consists in introducing some degree of stochasticity into the convective parameterization, either in an ad hoc fashion (Buizza et al., 1999; Lin & Neelin, 2000) or through a systematic derivation using first-physical-principle analogies (Berner et al., 2016; Khouider et al., 2010; Majda & Khouider, 2002; Plant & Craig, 2008). One of the goals of a stochastic scheme is to reintroduce the subgrid variability due to organized convection and break the QE constraint following a certain recipe. The stochastic multicloud model (SMCM) of Khouider et al. (2010), in particular, uses the mechanism of lattice particle interacting systems to build a birth-death stochastic process for the CAFs associated with the three main cloud types, congestus, deep, and stratiform, that characterize organized convective systems in the tropics (Johnson et al., 1999). Each lattice cell is assumed to be either occupied by a certain cloud type or a clear-sky site. The microcells then make random transitions from one state to another according to prescribed probability rules depending on the large-scale state. Various flavors of the SMCM have been successfully implemented and tested in both wave-dynamical models of intermediate complexity and in comprehensive state-of-the-art climate models (Dorrestijn et al., 2016; Frenkel et al., 2012; Goswami et al., 2017a; 2017b; Peters et al., 2017).

In Khouider (2014), a generalization of the SMCM framework that includes nearest neighbor interactions between the lattice sites has been proposed and analyzed. The SMCM with local interactions uses a prescribed local interaction potential, in addition to the external-large-scale potential. The local interactions provide in particular a framework through which the capability of convection to self-organize at the mesoscales can be represented. This includes the initiation and maintenance of mesoscale convective systems, squall lines, and supercells due to local processes such as variations in the ambient vertical shear, sea breeze, and orography (Khouider, 2014; Moncrieff, 1992). In Khouider (2014), an approximating multidimensional birth-death process for CAF is systematically derived, and the corresponding mean field equations were obtained, under the convenient assumption of uniform subgrid-scale mixing.

While distinct prognostic equations are provided for distinct cloud types, the Pan and Randall (1998) model does not allow interactions between various cloud types. Moreover, the CWF associated with each cloud type obeys a damped linear differential equation that is externally forced by the large-scale dynamics and assumes a small and fixed CAF. Inspired by the SMCM—with nearest neighbor interaction—framework introduced in Khouider (2014), here, we revisit the prognostic closure paradigm while considering two distinct but complementary modifications. First, we allow the CWFs associated with distinct cloud types to interact with each other, and second, the corresponding CAF is set to vary dynamically. The cloud-cloud interactions are achieved through a convolution kernel as in the original work of Arakawa and Schubert (1974) but restricted to up to three cloud types as in the SMCM framework. This constitute the first part of the present work. In the second part, we couple the CKE-CWF equations to the mean field equations for the CAF of Khouider (2014).

Pan and Randall (1998) showed that in the absence of coupling between the various cloud types and fixed CAF, the prognostic model undergoes damped oscillations independent of the strength of the large-scale forcing. In the first part of this work, when CAF is fixed as in Pan and Randall (1998), our results show that in the case of multicloud coupling, the stability of the CKE-CWF system changes drastically with the external parameters. In the case of two interacting clouds, the model exhibits a menagerie of back and forth bifurcations between regimes of asymptotically stable (damped) oscillations, limit cycles, and chaotic behavior, dependent on the strength of the coupling between the different cloud types. The two-cloud system is stable only when there is little to no interaction between the cloud types, or when one of the cloud types dominates in CAF. Linear analysis suggests that the same behavior is qualitatively maintained when we consider three interacting cloud types instead of two.

In the second part of the work, we include changes in CAF but assume there is only one cloud type. For the sake of simplicity, we assume that CAF is spatially homogeneous. The case with spatial variations in CAF will be reported elsewhere. We found that the stability, and number of equilibria, of the system are both affected by the environmental forcing. In some regimes of the forcing, the system admits three distinct equilibria, though only one or two are stable. Sometimes there is only a single equilibrium, but it is unstable, and the system yields either periodic oscillations (limit cycle) or chaotic behavior, depending on the forcing. Varying the environmental forcing periodically, as done in Pan and Randall (1998) to mimic oscillations in the large-scale dynamics (over a few minutes to a few hours), results in nontrivial behavior, which again encompasses asymptotic stability, limit cycles, and chaos. In the particular case of multiple equilibria, the system may remain near the equilibrium with large CAF or be driven by the forcing back and forth between the low CAF and high CAF equilibria, depending only on the period of oscillation of the forcing. While the slow oscillating forcing seemingly drives the CAF from the low to high CAF equilibria, on average, the solution undergoes rapid and strong oscillations during the transitions from low to high CAF and transitions between high to low CAF are more gentle, suggesting hysteresis. Forcing oscillations with moderate frequencies that are comparable to the CKE-CWF-CAF model's internal frequencies result in a phase locking where the CWF-CKE-CAF model oscillations and the forcing are synchronized. However, when the forcing is made to oscillate at a much faster rate, the CWF-CKE-CAF either locks itself near the more-stable high CAF equilibrium or undergoes chaotic behavior, depending of the range of the forcing variability and the associated bifurcations of the model.

While such dynamics is expected as from any three-dimensional nonlinear system of differential equations with changing parameters, our goal here is to demonstrate that this dynamical diversity occurs in the physically relevant parameter regimes, which the QE assumption fails to capture all together. Such behavior is reminiscent of the capability of cumulus convection to self-organize at multiple scales and transition between various regimes of mesoscale convective systems, squall lines, and scattered convection (Moncrieff 2010, 1992).

The paper is organized as follows. The governing equations of both the coupled CWF-CKE-mass flux and the multicloud mean field equations are discussed in section 2. Section 3 discusses the results summarized in the previous paragraph, and a discussion and a few concluding remarks are provided in section 4.

2. The Model Equations

2.1. The QE Closure and Its Relaxation

In their seminal paper, Arakawa and Schubert (1974) reduced the cumulus parametrization problem to one of finding the bulk convective mass flux, $M_c(z)$; the detrainment of clouds into the environment, $D(z)$; and the amount of liquid water $l(z)$ at the detrainment level. In this view, the bulk convective mass flux is defined as the total flux of mass that flows vertically through horizontal sections of all cloudy air portions σ_i:

$$M_c(z) = \sum_i \rho\sigma_i w_i,$$

where ρ is air density and w_i is the vertical velocity of the updraft inside the cloud section σ_i. To address this problem, Arakawa and Schubert (1974) introduced the notion of “spectral representation” of clouds or “convection plumes” where a single parameter λ, known as the entrainment rate, represents a class of such plumes that all detrain at the same level $z_D(\lambda)$. They make the intrinsic assumption that $z_D(\lambda)$ is a decreasing function of the parameter λ and define $\lambda_D(z)$ as the inverse function of $z_D(\lambda)$ so that $z = z_D(\lambda_D(z))$ and $\lambda = \lambda_D(z_D(\lambda))$. The bulk convective mass flux associated with all clouds that detrain above the level z is given by Arakawa and Schubert (1974) as

$$M_c(z) = \int_0^{\lambda_D(z)} \mathcal{M}(\lambda, z) d\lambda,$$

where $\mathcal{M}(\lambda, z)$ is the total mass flux of the subensemble of all clouds of type λ. This enables, in particular, an expression for the detrainment rate:

$$D(z) = -\mathcal{M}(\lambda_D(z), z)\frac{d\lambda_D(z)}{dz}.$$

More importantly, Arakawa and Schubert (1974) normalize the subensemble mass flux as

$$\mathcal{M}(\lambda, z) = M_b(\lambda)\eta(\lambda, z),$$

where $\eta(\lambda, z), 0 < \lambda \leq \lambda_{max}$ are (normalized) dimensionless vertical profile functions with $\eta(\lambda, z_b) = 1$ and $M_b(\lambda)$ is the mass flux of the subcloud ensemble at cloud base, $z = z_b$. While moist thermodynamic and cloud microphysics considerations define, for a given entrainment rate λ, the detrainment level $z_D(\lambda)$ as the vanishing buoyancy level, the vertical profile functions are assumed to satisfy the relations

$$\frac{\partial \eta(\lambda, z)}{\partial z} = \lambda \eta(\lambda, z), \qquad z_b \leq z \leq z_D(\lambda), \quad 0 < \lambda \leq \lambda_{max},$$

amounting to assuming plumes of conical shape. Although subcloud layer turbulent kinetic energy can be used to estimate the updraft vertical velocity at cloud base, the cloud base mass flux M_b requires the knowledge of both the vertical velocity and CAF associated with each cloud type λ. Arakawa and Schubert (1974) introduced instead the notion of a CWF, $A(\lambda)$, as the rate of kinetic energy generation per unit mass, so that the CKE, $\mathcal{K}$, associated with all clouds of type λ satisfies

$$\mathcal{K}(\lambda)t = A(\lambda)M_b(\lambda) - \mathcal{D}(\lambda), \tag{1}$$

where $\mathcal{D}(\lambda)$ is the dissipation rate of kinetic energy and $A(\lambda)$ is given by the weighted vertical integral of buoyancy, $B(z, \lambda)\eta(z, \lambda)$, of the updrafts associated with all clouds of type λ:

$$A(\lambda) = \int_{z_b}^{z_D(\lambda)} B(z, \lambda)\eta(z, \lambda)\, dz.$$

As such, the CWF depends exclusively on the environmental state in the cloud layer and the subcloud mixed layer.

According to Arakawa and Schubert (1974), the moist thermodynamic budget equations define the evolution equation for $A(\lambda)$, which takes the form

$$A(\lambda)t = \int_0^{\lambda_{max}} K(\lambda, \lambda')M_b(\lambda')\, d\lambda' + F(\lambda), \tag{2}$$

where the first term on the right-hand side represents the in-cloud contribution to the variation of $A(\lambda)$ and $F(\lambda)$ is the contribution from large-scale forcing. The kernel $K(\lambda, \lambda^{'})$ represents the influence of clouds of type $\lambda^{'}$ on clouds of type λ.

Arakawa and Schubert (1974) argue that "typically, the kernel $K(\lambda, \lambda^{'})$ is negative" and thus preexistence of clouds of any type are overall detrimental for further development of clouds of similar or any other type. In essence, they state that the dominant effect of the first-in-cloud term on the right-hand side of (2) is to decrease the CWF. The main argument used to arrive at this conclusion is that of "adiabatic warming of the environment due to subsidence induced by type $\lambda^{'}$ clouds," which is contributed directly by the convective mass flux part of the kernel. However, they also suggest that, through the detrainment term $D(z)$, shallower cloud types can increase CWF for deeper ones, essentially by cooling and moistening the environment. This is consistent with the SMCM paradigm (Khouider et al., 2010; Khouider & Majda, 2006) discussed below, by which clouds can grow vertically over time and transition from shallow to deep (Derbyshire et al., 2004; Hohenegger & Stevens, 2013; Johnson et al., 2015; Waite & Khouider, 2010; Wu et al., 2009).

By assuming that the "decrease" of the CWF by cumulus processes occurs on a much faster scale than the rate of change of the large-scale forcing, so that $A(\lambda)t \approx 0$ in (2), Arakawa and Schubert (1974) postulated a QE theory where the CWF is always in equilibrium with the large-scale forcing, although the large-scale variables are not necessarily in an equilibrium state. This basically assumes that there is a timescale separation between convective processes and the large-scale atmospheric dynamics. Empirical arguments have been provided for the smallness of $A(\lambda)t$ when the total CAF, $\sigma_c = \sum_i \sigma_i$, is assumed to be small (Arakawa & Schubert, 1974; Lord & Arakawa, 1980). These authors have also provided empirical estimates for the CWF-large-scale adjustment timescales, ranging from 10^3 to 10^4 s, that is, roughly 15 min to 3 hr. This can also be justified by the attributed stabilizing effect of the kernel $K(\lambda, \lambda^{'})$, provided it occurs on a faster timescale. The steady state equation for $A(\lambda)$ can then be inverted to obtain $M_b(\lambda)$ exclusively in terms of the large-scale forcing. Zhang and McFarlane (1995) use the same sort of argument, but they use convective available potential energy (CAPE; instead of CWF) and invoke a specific adjustment timescale τ_{adj}, or CAPE consumption timescale, of a few hours.

Despite wide support by the climate modeling community at that time, the QE theory has been criticized since its conception. Pan and Randall (1998), for instance, say that "the hypothesis of the CWF QE has been observationally tested by Arakawa and Schubert (1974); Grell, Kuo, and Pasch (1991); Kao and

Ogura (1987); Lord (1982); Lord and Arakawa (1980) among others," just before relaying a list of pitfalls that, they believe, discredit the QE theory. They invoke among other things the tight relationship between stratiform clouds and deep convection, with the former occupying large areas in space and being more persistent. On one hand, stratiform cloud decks provide direct and indirect forcing to cumulus clouds via stratiform-rain-evaporation-induced downdrafts and cloud radiative forcing, and on the other hand, deep convective clouds are the precursors for the development of stratiform anvils over timescales of just a few hours, that is, within the empirical convective adjustment time estimates provided above. In addition, cumulus processes are tightly connected with boundary layer turbulence (Pan & Randall, 1998), which also occurs on such timescales and shorter.

By defining $\mathcal{K}$ as the vertically integrated kinetic energy from cloud base to cloud top, Pan and Randall (1998) show that the CKE equation in (1) can be derived from the momentum equations (not shown here) when the shear production terms are neglected. The dominant buoyancy contribution itself becomes the first term on the right-hand side of equation (1). They further assume that the dissipation term takes the simple linear form

$$\mathcal{D}(\lambda) = \frac{1}{\tau_D}\mathcal{K}(\lambda), \tag{3}$$

assuming a constant dissipation timescale τ_D independent of the cloud type, and propose an alternative closure for the equations in (1) and (2), forgoing the QE assumption. In particular, they derive a relationship between $\mathcal{K}$ and M_b, as follows.

The horizontal average of the vertical velocity, w, over a large-scale area that contains a large ensemble of individual clouds (possibly of various types) satisfies

$$\bar{w} = \sigma_c w_u + (1 - \sigma_c) w_d, \tag{4}$$

where the overbar represents the horizontal average, σ_c is the area fraction of the updrafts, w_u is the average updraft velocity within the clouds, and w_d is the average downdraft velocity within the environment.

If w' denotes the turbulent fluctuations of vertical velocity, that is, $w' = w - \bar{w}$, then assuming the top-hat approximation,

$$w = \begin{cases} w_u, & \text{within the updraft region} \\ w_d, & \text{outside the updraft region} \end{cases},$$

leads to

$$\overline{w'^2} = \sigma_c(w_u - \overline{w})^2 + (1 - \sigma_c)(w_d - \overline{w})^2. \tag{5}$$

Combining the equations in (4) and (5) yields

$$\overline{w'^2} = \sigma_c(1 - \sigma_c)(w_u - w_d)^2 \approx \sigma_c w_u^2, \tag{6}$$

where the last approximation is made under the assumptions that $\sigma_c \ll 1$ and $|w_u| \gg |w_d|$. The first approximation could be relaxed in the future to accommodate a resolution aware parameterization, to take full advantage of the predicted value of σ_c by the SMCM of Khouider et al. (2010). (One could instead use $\overline{w'^2} \approx \sigma_c(1 - \sigma_c)w_u^2$.)

We now invoke the relation

$$M_c(z, \lambda) := \sigma_c(\lambda)\rho w_u(z, \lambda) = M_b(\lambda)\eta(z, \lambda) \tag{7}$$

for the bulk mass flux associated with all clouds of a given type λ. Unlike Pan and Randall (1998), however, we maintain the dependence of CAF on the cloud type parameter λ. Simple algebra based on (6) and (7) shows that the vertical kinetic energy density is given by

$$\frac{1}{2}\rho\overline{w'^2} = \frac{M_c^2}{2\rho\sigma_c}.$$

Integrating this equation from cloud base to cloud top and using (7), we deduce that the vertically integrated total kinetic energy associated with all clouds of type λ satisfies

$$\mathcal{K}(\lambda) = \frac{\alpha(\lambda)}{\sigma_c(\lambda)}\left(M_b(\lambda)\right)^2, \tag{8}$$

where

$$\alpha(\lambda) = \frac{1}{2\varepsilon(\lambda)}\int_{z_b}^{z_D(\lambda)} \frac{\eta^2(z,\lambda)}{\rho(z)}dz.$$

Here $\varepsilon(\lambda)$ is the fraction of vertical to total kinetic energy, which is assumed to be fixed according to statistical theory of turbulence (Pan & Randall, 1998).

The four equations in (1), (2), (3), and (8) form a closed system of equations for $\mathcal{K}$ and A, or equivalently, M_b and A, with unknown parameters α and σ_c, which Pan and Randall (1998) call the prognostic closure for the Arakawa-Schubert cumulus parameterization. It provides an alternate cumulus scheme, which they test and evaluate against the standard QE-based Arakawa-Schubert scheme (Pan & Randall, 1998; Randall & Pan, 1993). Consistent with the assumption that the kernel in (2) acts solely to reduce CWF, Pan and Randall (1998) write a simple system of equations for A and M_b, where the kernel K is assumed to be a single negative constant ignoring coupling between different cloud types. Namely, they set $K = -J$, where J is a positive parameter and obtain the following system:

$$\begin{aligned} \frac{dA}{dt} &= -JM_b + F \\ \frac{d\mathcal{K}}{dt} &= M_bA - \frac{1}{\tau_D}\mathcal{K} \\ \mathcal{K} &= \frac{\alpha}{\sigma}M_b^2. \end{aligned} \tag{9}$$

Here the dependence on λ is ignored for simplicity. The linear system in (9) reduces to a forced damped oscillator for A, or equivalently M_b alone:

$$\frac{d^2M_b}{dt^2} + \frac{1}{2\tau_D}\frac{dM_b}{dt} + \frac{\sigma J}{2\alpha}M_b = F,$$

which yields damped oscillations when J is large enough, provided the forcing F does not resonate with the system's internal modes whose frequencies are given by $\omega_i = \frac{1}{2}\sqrt{2\sigma J/\alpha - \tau_D^{-2}/4}$.

This may be viewed as further justification for the QE theory, provided the term $\sigma J/\alpha$ is sufficiently large compared to the characteristic timescale of the forcing. Nonetheless, Pan and Randall (1998) argue that the existence of such oscillations, although damped, will provide the cumulus scheme its own memory, which contradicts the QE assumption. Here, we take a further step by first considering cross terms for the A-equation in (9), coupling clouds of various types. To include both the negative and positive effects of various cloud types on each other and yet to do so in a simple finite situation, we assume that the kernel K reduces instead to a matrix of finite size, corresponding to a fixed number of cloud types, as a discretization of equation (2). Namely, we consider the scenarios of two and three cloud types. Following Arakawa and Schubert (1974), we assume that shallow cloud types favor the formation of deeper ones, while deep cloud types suppress the potential for shallower cloud types. In particular, we show that under these circumstances, the coupled system exhibits unstable oscillations, especially when the coupling between clouds is significant and when the corresponding CAF parameters are comparable. In addition, we introduce and couple the CKE and CWF equations to prognostic equations for the CAF of various cloud types, based on the mean field limit of a SMCM with nearest neighbor interactions (Khouider, 2014). The multicloud model mean field CAF equations are introduced in the following section.

2.2. The SMCM for the CAF and Its Mean Field Limit

The stochastic mulicloud model (SMCM), first introduced in Khouider et al. (2010), is based on the theory of interacting particles, in a heat bath, of statistical mechanics (Liggett, 1999). A fine rectangular lattice, of $N \times N$ microscopic cells, is superimposed on each of the climate model's horizontal grid cells, and an order parameter, X_t, takes discrete values 0, 1, 2, or 3, at any given time $t > 0$, on each lattice cell, according to whether the underlying site (lattice cell) is clear sky or occupied by a congestus, deep, or stratiform cloud type.

$$X_t(x) = \begin{cases} 0 & \text{if } x \text{ is clear sky} \\ 1 & \text{if } x \text{ is occupied by a congestus cloud type} \\ 2 & \text{if } x \text{ is occupied by a deep cloud type} \\ 3 & \text{if } x \text{ is occupied by a stratiforms cloud type} \end{cases} \tag{10}$$

Congestus clouds are cumulus decks that typically develop in the lower troposphere and detrain below the freezing level, when the middle troposphere is relatively dry. Deep convective clouds are cumulonimbus clouds that reach 10 to 15 km. Stratiform clouds develop in the upper troposphere in the wake of deep convection (Johnson et al., 1999; Khouider et al., 2010). The order parameter X_t makes random jumps as a Markov process, from one discrete state to another with high probability according to whether the large-scale state is favorable for clear sky or for the development of congestus, deep, or stratiform cloud types. This is achieved by assuming that the transition probabilities depend explicitly on key large-scale predictors, namely, CAPE (a concept close to the CWF) and midlevel moisture. For a small time lapse, Δt, we have

$$\text{Prob}\{X_{t+\Delta t}(x) = k | X_t(x) = l\} = R_{kl}\Delta t + O(\Delta t),\ \ k, l = 0, 1, 2, 3. \tag{11}$$

For the sake of simplicity, Khouider et al. (2010) neglected interactions between lattice sites by making the transition rates R_{kl} depend exclusively on the large-scale predictors—independent on the realizations of X_t outside the underlying site x. This simplification enabled the derivation of a coarse-grained stochastic birth-death process for the CAFs associated with each cloud type, in closed form without any further assumptions, and its successful validation and implementation in a hierarchy of climate models (Bergemann et al., 2017; Deng et al., 2015; Dorrestijn et al., 2016, 2013; Frenkel et al., 2012; Goswami et al., 2017a, 2017b; Peters et al., 2013, 2017).

Khouider (2014) provides a more complete derivation of a coarse-grained birth-death process for the SMCM with nearest neighbor interactions. In Khouider (2014), the transition rates in (11) are given by Arrhenius-type dynamics that are in partial detailed balance with respect to the Gibbs measure

$$G(X_t) = Z \exp\left(-k_B^{-1} T_B^{-1} H(X_t)\right). \tag{12}$$

Here,

$$H(X_t) = -\frac{1}{2}\sum_{x,y} U[x, y, X_t(x), X_t(y)] X_t(x) X_t(y) + \sum_x h(X_t(x)) \tag{13}$$

is a Hamiltonian energy that includes the effect of a local interactions potential U and an external potential h, k_B is the Boltzmann constant and T_B temperature of the heat bath, and Z is a normalization constant known as the partition function (Khouider, 2014). To restrict the local interactions to nearest neighbors, the internal potential takes the form

$$U(x, y) = \begin{cases} U_0 & \text{if} |x-y| \le r_0 \\ 0 & \text{elsewhere} \end{cases}, \tag{14}$$

where $|x - y|$ denotes the distance between the two lattice cells, x, y and $\sqrt{2} \le r_0 < 2$, such that the eight surrounding neighbors are taking into account, and U_0 depends only on the values of $X_t(x)$ and $X_t(y)$. Specifically, the rates R_{kl} depend on the energy differences

$$\Delta_{k,l} H(x) = H[X_t | X_t(x) = l] - H[X_t | X_t(x) = k], \qquad k, l = 0, 1, 2, 3,$$

where $H[X_t | X_t(x) = l]$ denotes the Hamiltonian energy conditional on $X_t(x) = l$, $l = 0, 1, 2, 3$. The transition rates are partially constrained by detailed-balance-type conditions so that the Markov process is ergodic with a limiting distribution given by (12). The interested reader is referred to Khouider (2014) for precise expressions.

While in the present study both h and U_0 in (13) and (14) are used as fixed parameters, in an actual parameterization they depend explicitly on key large-scale dynamical and thermodynamical quantities that are known to directly influence the organization of convection on various scales. Many meteorological parameters such as CAPE, convective inhibition (CIN), midlevel moisture, vertical shear, orography, and land-sea thermal contrast can be used to define the quantities h and U (Bergemann et al., 2017; Cardoso-Bihlo et al., 2019; Khouider, 2014). The effect of vertical shear and (unresolved) land-sea contrast can be used to break the symmetry in U (14) and allow self organization and propagation of mesoscale systems at the unresolved scales.

In the limit of a large number of microscopic sites, the dynamics of the multicloud CAF can be approximated by the deterministic mean field equations (Khouider, 2014),

$$\begin{aligned}\frac{d\sigma_1}{dt} &= \alpha_{01}\sigma_0 - (\alpha_{10} + \alpha_{12} + \alpha_{13})\sigma_1,\\ \frac{d\sigma_2}{dt} &= \alpha_{02}\sigma_0 + \alpha_{12}\sigma_1 - (\alpha_{20} + \alpha_{23})\sigma_2,\\ \frac{d\sigma_3}{dt} &= \alpha_{03}\sigma_0 + \alpha_{13}\sigma_1 + \alpha_{23}\sigma_2 - \alpha_{30}\sigma_3.\end{aligned} \tag{15}$$

Here σ_i is the area fraction of cloud type i, $i = 1, 2, 3$, and $\sigma_0 = 1 - \sigma_1 - \sigma_2 - \sigma_3$ is the cloud free (or clear sky) area fraction while $\alpha_{kl}, k, l = 0, 1, 2, 3$, are functions of the σ_i', represent the fractional transition rates, from state k to state l, and are obtained in terms of the transition rates R_{kl} (11) of the Markov process (Khouider, 2014). Partial derivatives are used in (15) because the σ's are in principle assumed to depend on time as well as on the space variables (x, y). Only the case of spatial homogeneity is considered herein for the sake of simplicity.

Following Khouider (2014), we have

$$\alpha_{kl} = \tilde{R}_{kl}e^{\Gamma_{kl}(\sigma)} = \frac{1}{\tau_{kl}}h_{kl}e^{\Gamma_{kl}(\sigma)}, \quad k \neq l, \tag{16}$$

where τ_{kl} is the timescales associated with the corresponding transitions and h_{kl} are the corresponding external potential values, which depend on the large-scale atmospheric conditions, while the Γ_{kl} functions carry the dependence on the σ values. According to Khouider (2014), the Gamma functions are convolutions with the internal potential U:

$$\Gamma_{kl}(\sigma) = \Gamma_{0l}(\sigma) - \Gamma_{0k}(\sigma), \qquad \text{and} \qquad \Gamma_{0k} = \sum_{l=1}^{3} U_{kl} * \sigma_l, \tag{17}$$

where the convolution operation, . * ., is approximated on a lattice by the expression

$$U_{kl} * \sigma_l(x, y) \approx U_{0,kl}\left[\sum_{i,j=-1}^{1} \sigma_l(x + i\Delta, y + j\Delta) - \sigma_l(x, y)\right], \tag{18}$$

where Δ is the size of the lattice mesh. Here, $U_{0,kl}$ is the background value of U_{kl} introduced in (14).

On a lattice of size N, the ODEs in (15) define a large system of $3N$ nonlinear differential equations, which approximates a system of three integro-differential equations that would have been obtained if the actual convolution operation was used instead of the approximation in (18). Nonetheless, here we consider only the simple case where the σ's are uniform over the lattice; that is, we neglect spatial variations and reduce the system in (15) to the case when $N = 1$. The case when σ varies in space will be analyzed reported elsewhere. In the uniform case, the convolution approximation becomes

$$U_{kl} * \sigma_l(x, y) \approx 8U_{kl}^0\sigma_l = U_{kl}^0\sigma_l. \tag{19}$$

In the last equality, we absorbed the multiplier 8 into U_{kl}^0 for convenience.

3. Results

3.1. Linear Stability Analysis With Fixed Area Fraction

We first consider linear stability analysis of the CKE-CWF equations in (1) and (2) when the area fraction, σ_λ, is fixed, as in Pan and Randall (1998). However, we provide structure to the kernel to allow cross coupling between distinct cloud types. For simplicity, and consistent with the trimodal character of tropical convection (Johnson et al., 1999; Khouider & Majda, 2006), we assume either two or three cloud types (shallow and deep or shallow, congestus, and deep, for example). In this case, the governing equations for the vectors A and M_b of $\mathbb{R}^n, n = 2, 3$, take the form

$$\begin{aligned} \frac{dA_\lambda}{dt} &= (K * M_b)_\lambda + F_\lambda \\ \frac{dM_{b,\lambda}}{dt} &= \frac{\sigma_\lambda}{2\alpha_\lambda}A_\lambda - \frac{1}{2\tau_{D,\lambda}}M_{b,\lambda},\ \lambda = 1, 2 \text{or} \lambda = 1, 2, 3, \end{aligned} \tag{20}$$

where the convolution $K * M_b$ becomes simply a matrix vector multiplication. We assume linear dissipation of CKE with a dissipation timescale, $\tau_{D,\lambda}$, depending on the cloud type as in Pan and Randall (1998). Consistent with the intuition that, through the convolution kernel (Arakawa & Schubert, 1974), the presence of clouds of a given type decreases the work function for shallower cloud types and increases it for deeper ones. We thus assume that the entries of K on and above the diagonal are negative and those below the diagonal are positive. Thus, for $n = 2$, we set

$$K = \begin{bmatrix} -J_{11} & -J_{12} \\ {}_J21 & -J_{22} \end{bmatrix},$$

and for $n = 3$, we have

$$K = \begin{bmatrix} -J_{11} & -J_{12} & -J_{13} \\ J_{21} & -J_{22} & -J_{23} \\ J_{31} & J32 & -J_{33} \end{bmatrix},$$

where the entries $J'_{\lambda\lambda}$ are nonnegative parameters. The scaling analysis reported in Appendix A at the end of the paper shows that the system in (20) is well balanced when the dynamical variables assume the following realistic dimensional units based on estimates provided in these seminal papers (Arakawa & Schubert, 1974; Lord & Arakawa, 1980; Lord, 1982; Pan & Randall, 1998):

$$[J] = 100\frac{\text{m}^4}{\text{kg s}^2}, [M_b] = 10^{-3}\frac{\text{kg}}{\text{m}^2\ \text{s}}, \left[\frac{\alpha}{\sigma}\right] = 10^8\frac{\text{m}^4}{\text{kg}}, [\tau_D] = [t] = 1000\text{s}, [A] = 10^2\frac{\text{m}^2}{\text{s}^2}. \tag{21}$$

Here the square brackets [.] denote the dimensional scale of the corresponding variable. This makes the above equations well suited for linear analysis in the physically relevant regime. In particular, it allows us to pick physical values for the free parameters $J_{\lambda \quad \lambda'}, F_\lambda, \beta_\lambda = \frac{\sigma_\lambda}{2\alpha_\lambda}$ and $\tau_{D,\lambda}$, around unity. For convenience, we fix $\tau_{D,\lambda} = 0.5$ and vary the rest of the parameters.

3.1.1. Two Cloud Types

We start with the case of two interacting cloud types, 1 and 2, say shallow and deep. Based on the dimensional analysis provided in the appendix at the end of the paper, the parameters and variables in (20) when measured in the dimensional units in (21) take values around unity. To illustrate the behavior of the corresponding dynamical system, we consider the numerical example where

$$K = \begin{bmatrix} -3 & -2 \\ 0.5 & -1 \end{bmatrix}, \quad \beta_\lambda := \frac{\sigma_\lambda}{2\alpha_\lambda} = 2.5, \quad \tau_{D,\lambda} = \frac{1}{2}, \quad F_\lambda = 0, \qquad \lambda = 1, 2, \tag{22}$$

around which the parameters $J'_{\lambda\lambda}$ and β_λ are systematically varied. The real and imaginary parts of the eigenvalues of this system are plotted on the four panels of Figure 1, when the coefficients $J'_{\lambda\lambda}$ are varied one at a time. We recall that in this setting, eigenvalues with positive real part amount to an instability of the equilibrium at the origin while the imaginary parts represent the frequency of oscillating modes.

Unlike the case of a single-cloud type (or noninteracting clouds) considered by Pan and Randall (1998), we can easily see, from Figure 1, that in addition to the intrinsic oscillations, the system is frequently unstable.

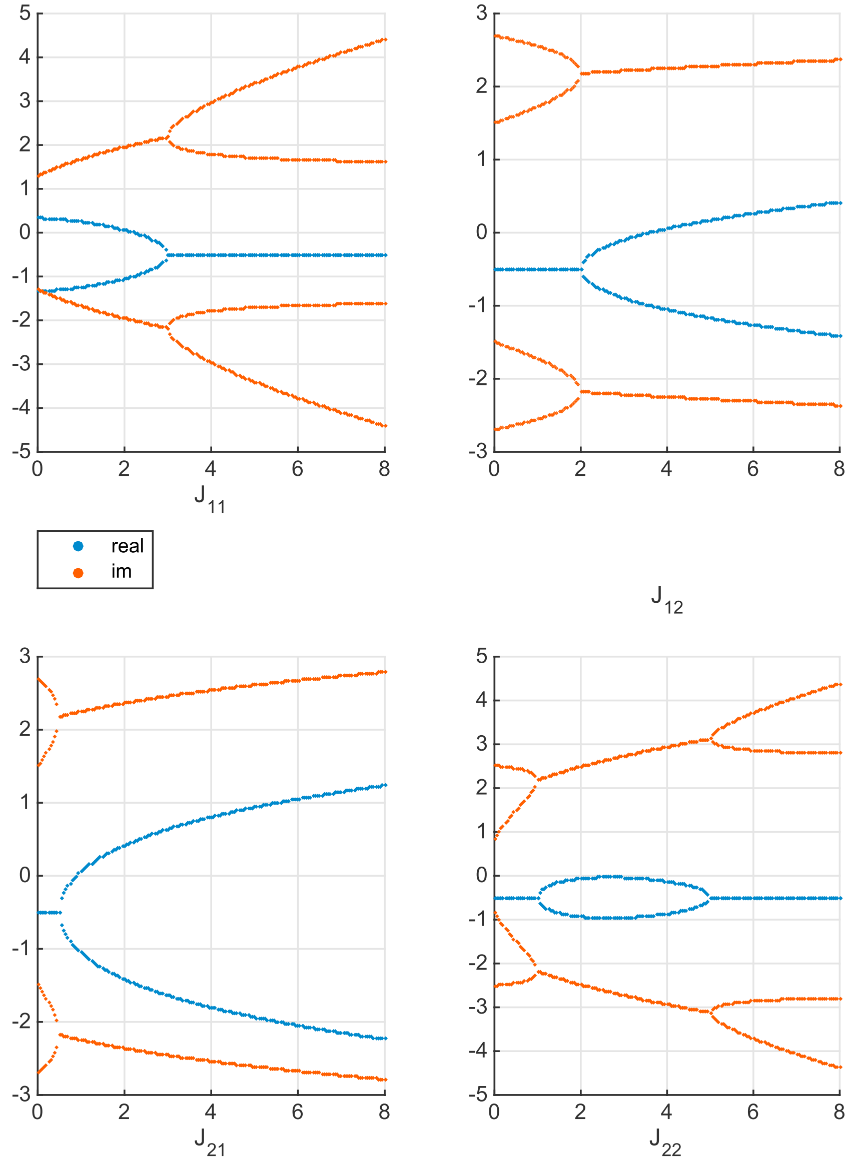

Figure 1. The real and imaginary parts of the eigenvalues of the two-cloud-type system when the entries $J'_{\lambda\lambda}$ are varied one at a time while the rest of the parameters are kept as in (22). The value of $J'_{\lambda\lambda}$ is displayed on the x axis of the corresponding panel.

In fact, an interesting pattern seems to emerge from Figure 1. For relatively small off-diagonal entries of K, the system is stable, but as the absolute value of one of these entries increases, the system's stability decreases until it suddenly becomes outright unstable. This turns out to be the case in general. As the only measure of the coupling between the two cloud types, if the off-diagonal entries of K are 0 or small enough relative to the diagonal entries, the system is approximately made up of two independent versions of the 1-cloud model. This is always stable as discussed above, consistent with the work of Pan and Randall (1998). We can therefore see that the instability of the system grows with the cloud-cloud coupling.

We now consider variations in the parameters β_λ, $\lambda = 1, 2$. Since the σ_λ's should sum to no more than unity, it makes sense to vary the β's while keeping their sum fixed.

Extensive numerical tests (not all shown here) reveal that when the sum $\beta_1 + \beta_2$ is fixed to small-to-moderate values, slightly less than five units, the parameter regime in (22) remains particularly stable, mainly because the off-diagonal entries of the K-matrix are sufficiently small. Nonetheless, an interesting and consistent structure of the stability diagram, as illustrated on the left panel in Figure 2 for the case $\beta_1 + \beta_2 = 5$, emerges

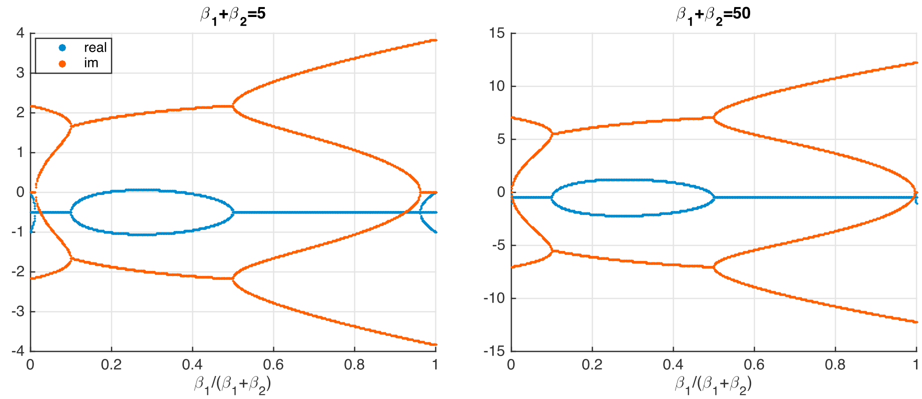

Figure 2. Same as in Figure 1 but β_1 and β_2 are varied instead. Left, $\beta_1 + \beta_2 = 5$. Right, $\beta_1 + \beta_2 = 25$.

with bifurcations around the points $\beta_1/(\beta_1 + \beta_2) = 0.1$ and $\beta_1/(\beta_1 + \beta_2) = 0.5$. Between these two limits the real part curves make a "bubble" that comes close to crossing the x axis near the midpoint of these limits and eventually does cross it when $\beta_1 + \beta_2 = 5$ as can be seen in Figure 2. Our tests reveal that increasing $\beta_1 + \beta_2$ by a factor of p stretches the real and imaginary parts of the eigenvalues by a factor of $\sqrt{p}$ about their respective centers (except for the bifurcation limits, which do not get stretched). This means that sufficiently increasing $\beta_1 + \beta_2$ creates or enlarges the region of instability, as revealed by the right panel in Figure 2 when $\beta_1 + \beta_2 = 25$. Such values of $\beta_1 + \beta_2$ may seem excessive. However, according to the scaling analysis in Appendix A, the β values are based on a fixed area fraction of around 0.01 (Pan & Randall, 1998). Thus, increasing both β_1 and β_2 by a factor of 10 to 20 amounts to increasing the reference area fraction by the same factor that is reasonable, especially, in the case of climate models at gray-zone resolutions of about 10–20 km.

In general, as it turns out, the system is always stable except possibly in a small region "in the middle," where the coefficients β_1 and β_2 can be said to be comparable. This amounts to concluding that the two-cloud system will become stable whenever one or the other CAFs dominates. On an intuitive level, this is mathematically consistent with the intuition that the cloud-cloud coupling drives the instability. If both cloud types are present, with sufficient area fraction, then they will interact with one another. If they meaningfully interact with each other and lead to instability, then they must both be present in sufficient amounts.

3.1.2. Three Cloud Types

We now consider the system in (20) in the case of three interacting cloud types, shallow, congestus, and deep, exemplified by the following parameter regime around which the system's parameters are varied. Let

$$K = \begin{bmatrix} -0.5 & -1 & -2 \\ 2 & -1 & -2 \\ 2 & 0.1 & -0.5 \end{bmatrix}, \quad \beta_\lambda = 2.5, \quad \tau_{D,\lambda} = 0.5, \quad F_\lambda = 0, \ \lambda = 1, 2, 3 \tag{23}$$

be the standard parameter regime for this case, around which the key parameters $J_{\lambda,\lambda}$ and β_λ are varied.

Similarly to the two-cloud-type case, we compute the eigenvalues of the 6×6 matrix when its entries vary one or two at a time. Broadly speaking, the 6×6 system behaves in the same way as the two-cloud-type 4×4 system: The strength of cloud-cloud coupling always leads to instability whether it is through assuming strong off-diagonal elements of the kernel K or by compensation with comparable β parameters. This is illustrated in Figure 3 where the entries of K are systematically varied one at a time while the rest of the parameters are fixed as in (23). As we can see, although the system is already unstable to begin with, increasing the off-diagonal entries of K leads to a decrease in strength of the instability, which eventually yields stability as illustrated by the J_{11} panel.

The second point about the β parameters also remains: If the β parameters are made comparable, the system is merely unstable. Similarly to the 2 clouds case, we fix the sum $\beta_1 + \beta_2 + \beta_3$ and one of the parameters β_λ and vary the ratio $\beta_\lambda/(\beta_1 + \beta_2 + \beta_3)$. As illustrated in Figure 4, the system may only be stable when one of the β parameters becomes dominant, which leads to a situation of a quasi-decoupling as in the limits when $\beta_1 = 0, \beta_2 = 50, \beta_3 = 25$ and $\beta_3 = 50, \beta_1 = 0, \beta_2 = 25$, respectively, on the left and right panels of Figure 4.

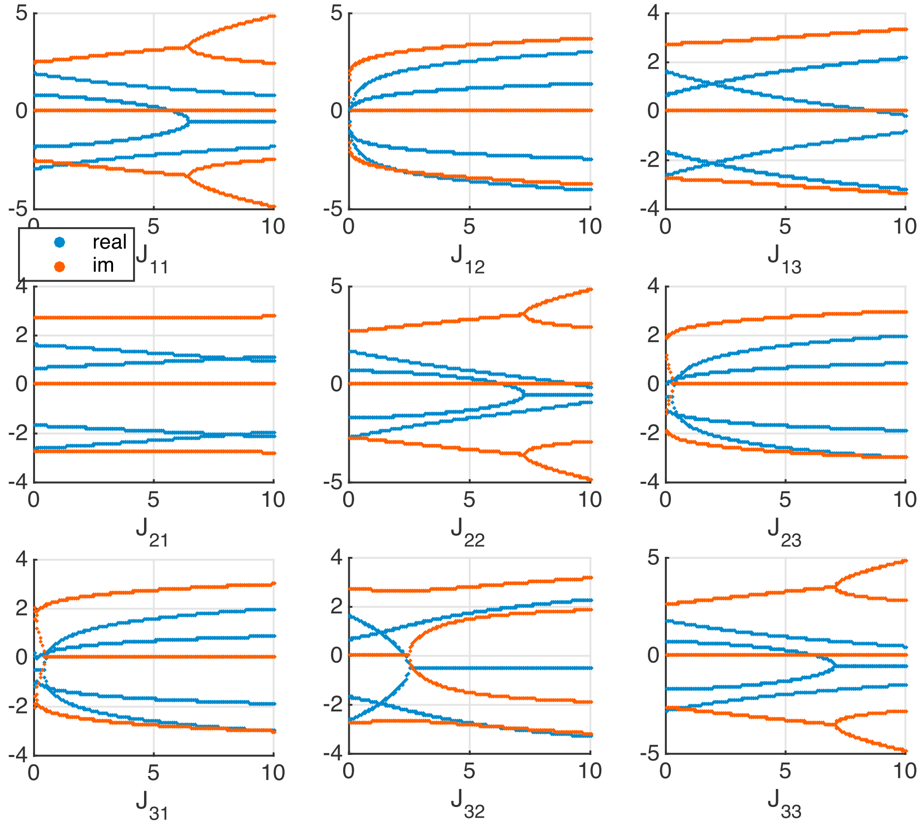

Figure 3. Real and imaginary parts of the eigenvalues of the system (23) when the entries of K are varied one at a time. The J entry that varied is indicated on the bottom of each panel while the x axis spans the range of its values.

3.2. The Coupled CWF-CKE-CAF Model

As demonstrated above, the CWF-CKE equations are stable only when the diagonal entries of the cloud-cloud interaction kernel K dominate, or one of the cloud types dominates over the others. This in essence confronts the results of Pan and Randall (1998) who suggested that the diagnostic closure equations (1)–(8) lead to damped oscillation behavior, by assuming that the cloud-interaction kernel serves essentially to damp the CWF. However, they also stress that the existence of oscillations allows for some memory in the cloud model and possibility for resonance with the large-scale forcing when the CKE-CWF oscillation timescales are not too fast compared to the large-scale variability. While one may argue that the damping effect of the kernel is the typical physical regime and that cases of strong coupling are perhaps more of an exception, the Pan and Randall model behavior is constrained to having a fixed CAF. To illustrate the plausible impact of having a variable CAF, here, we couple the CKE-CWF (or rather the $M_b - A$ equations in (9)) to the SMCM mean field equations in (15). This allows the CAF to vary at the same time as the mass flux and the CWF. For the sake of simplicity, we consider only the case of a single cloud type—amounting to reinforcing back the damping effect of the cloud interaction kernel as Pan and Randall have assumed. Nevertheless, as we will see in this section, this is enough to discover interesting-unstable dynamical behavior, including multiple equilibria, limit cycles, and chaos, especially when the forcing is made to vary.

To begin, we assume that the external potential h in (12) depends solely on the CWF A, as detailed below. Based on the equations in (9) and (15) through (19), we obtain the following CKE-CWF-CAF ($M_b - A - \sigma$)-coupled system for the case of a single cloud type.

$$\begin{aligned}
\frac{dA}{dt} &= -JM_b + F \\
\frac{dM_b}{dt} &= \frac{\sigma}{d\sigma}\beta A - \frac{1}{\tau}M_b \\
\frac{d\sigma}{dt} &= \frac{1}{\tau_c}e^{\gamma A - H}e^{U_0\sigma}(1-\sigma) - \frac{1}{\tau_c}\sigma.
\end{aligned} \tag{24}$$

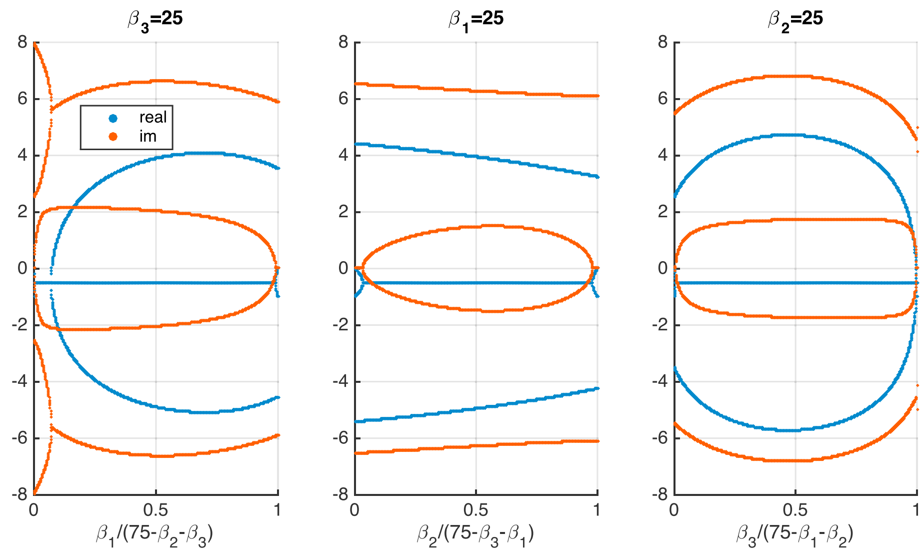

Figure 4. Real and imaginary parts of the eigenvalues of the three-cloud-type system in (23) as the β parameters are varied while their sum is kept constant: $\beta_1 + \beta_2 + \beta_3 = 75$. Left, $\beta_3 = 25$; middle, $\beta_1 = 25$; right, $\beta_2 = 25$.

Here J, F, τ assume our established nondimensional units (all on order unity) and $\gamma, U_0 := U^0_{kl}, \tau_c$ are new parameters, specific to the SMCM. In particular, we introduced the reference CAF scale $\hat{\sigma} = 0.01$ and set $\beta = \frac{\hat{\sigma}}{2\alpha}$ to be a dimensional constant assuming the corresponding reference value in (21). τ_c can be readily expressed in the same units as τ without changing anything to these equations. For simplicity, we assume $\tau = \tau_c = 1$. We note that the factor $e^{\gamma A - H}$ in the σ equation represents the effect of the external potential on the creation and growth of σ, where γ is a scaling factor and H is a convective inhibition threshold. Preliminary tests reveal that $\gamma = 1, H = 5$, and U_0 varying from $U_0 = 0$ (meaning no local interactions) to $U_0 = 10$ (strong local interactions) yield physically reasonable equilibrium solutions, especially in terms of the CAF. For convenience, the coupled model parameters and their physical significance are regrouped in Table 1.

3.2.1. Case of Constant Forcing

The system in (24) is nonlinear. We thus need to first find its equilibrium solution (or solutions) depending on the forcing F (and the other parameters of course) and then linearize it and study its linear stability accordingly. We finally investigate its nonlinear behavior via numerical simulations.

Simple algebra shows that the equilibrium solutions of (24) satisfy

$$M_b = \frac{F}{J}, A = \frac{\hat{\sigma}}{\sigma\beta\tau}\frac{F}{J}, \mathcal{G}(\sigma) := Ce^{D\sigma + E/\sigma}(1-\sigma) - \sigma = 0, \tag{25}$$

Table 1
List of Physical Parameters and Their Values (in Dimensional Units in Equation (21)) for the Coupled CKE-CWF-CAF Model

Parameter	Description	Value
J	CWF interaction kernel	0.1
F	CWF environmental forcing	Varies
τ	CKE (cloud base mass flux) dissipation timescales	1
β	CKE production coefficient	1
γ	Scaling factor for CAF growth rate	1
H	CAF growth threshold (convective inhibition)	5
U_0	Strength of local interaction potential	Varies, typically, 3,7,8
τ_c	CAF timescale	1
$\hat{\sigma}$	CAF reference scale	0.01

Note. CKE = cumulus kinetic energy; CWF = cloud work function; CAF = cloud area fraction.

where C, D, E are positive constants that depend on the parameters F, J, γ, and H. Because $\mathcal{G}(\sigma)$ is $+\infty$ at $\sigma = 0$ and -1 at $\sigma = 1$, there is a positive, odd, number of solutions to this equation that are easily computed using a root-finding numerical technique (Khouider & Bihlo, 2018; Majda & Khouider, 2002).

We will throughout the rest of this paper mainly consider the parameter regime (or family of parameter sets) depicted in Table 1. Other regimes are qualitatively similar. Considering this regime allows us to vary only U_0 and F in order to gather information about the behavior of the system. On physical grounds M_b should always remain nonnegative, but there is nothing preventing it from being negative. Our tests (not shown here) demonstrate that since at equilibrium $M_b \geq 0$ (because F is assumed to be always nonnegative), replacing M_b by $\max(M_b, 0)$ in the A-equation (first equation in (24)) makes very little difference, and only in a few marginal cases. It mainly extends the transient period, before the solution reaches the same statistical steady state, as illustrated next.

We consider three typical cases of the parameter regimes in Table 1, corresponding to $U_0 = 3$, $U_0 = 7$, and $U_0 = 8$ and report in Figure 5 the equilibrium values of σ and A. Figure 5 also shows the associated real and imaginary parts of the eigenvalues of the Jacobian matrix of the CKE-CWF-CAF system (24) around each equilibrium solution, when F is varied from 0 to up to 80. Since the equilibrium value of M_b varies merely linearly with F, it is not depicted in Figure 5 for the sake of streamlining. We recall here that U_0 represents the strength of the local interaction potential of the microscopic-cloud model. As such, the three regimes depicted in Figure 5 correspond to a case of weak local interactions with $U_0 = 3$, a case of strong local interaction with $U_0 = 7$ and a case with stronger local interactions with $U_0 = 8$.

As shown in Figure 5, when $U_0 = 3$ the system has only one equilibrium for all $F \geq 0$. It starts near a zero CAF value, $\sigma \approx 0$ when $F = 0$; increases almost linearly; and then smoothly curves down and transitions to and saturates near $\sigma = 1$ when $F \geq 40$. Interestingly, the stability of the system also bifurcates from being stable for small values of σ corresponding roughly to $F \leq 5$, to forming an instability bubble for intermediate values of σ within the range $5 \leq F \leq 40$, to becoming stable again, for $F \geq 40$ and making the equilibrium value of CAF nearly one, $\sigma \approx 1$. Curiously, the CWF variable A accordingly undergoes some regime transitions. It starts by a rapid increase with F when F remains small, it plateaus in the range of F corresponding to the instability bubble, and then it picks up again and increases almost linearly, afterward, with an intermediate sloping value.

As expected from the mean field CAF model (Khouider & Bihlo, 2018; Majda & Khouider, 2002), the cases $U_0 = 7$ and $U_0 = 8$ present regimes of multiple equilibria. In the first case, the system begins with a single equilibrium that is near $\sigma = 0$ and transitions to a regime with three equilibrium points when F is roughly between 6 and 7.5, to a regime with again a single equilibrium but near $\sigma = 1$. To ease the exposition, in cases with multiple equilibria, the equilibrium point near $\sigma = 0$ is referred to as the lower equilibrium, the one near $\sigma = 1$ is called the upper equilibrium and the one in between, when there are three equilibria, is designated as the middle equilibrium. From Figure 5, we see that the lower equilibrium bifurcates from being stable to being unstable, near $F \approx 2.5$, before the multiple equilibria regime is first reached near $F = 6$. During the new regime both the lower and middle equilibria are unstable, while the upper equilibrium is always stable, including when the system exhibits the multiple equilibria regime, for $F \geq 7$. The second case with $U_0 = 8$ starts off within the multiple equilibria regime and smoothly transitions to a regime where only the upper equilibrium survives. While the upper equilibrium is again always stable and the middle equilibrium always unstable, the lower equilibrium itself starts off stable for $F \leq 1$ or so and then becomes unstable until it disappears at the second bifurcation point near $F = 5.5$.

Similarly to the case $U_0 = 3$, in the two cases with multiple equilibria, the CWF equilibrium value follows the same pattern as the CAF values. It undergoes various dynamical regimes as the system bifurcates from stable to unstable regimes and also from single to multiple equilibria regimes. First, the lower equilibrium seems to have a larger CWF value than both the middle and upper equilibrium, consistent with (25). Somehow, the regime with lower mean CAF values is associated with a state of larger potential energy, and it is thus potentially more turbulent. Second, the CWF of the lower equilibrium increases rapidly near $F = 0$ when the system is stable, then plateaus and reaches a maximum in the regions where the corresponding equilibrium point is unstable.

Although the results are not shown here, we have extensively explored the parameter space by varying J, β, γ, H, and so forth. Our results indicate that the three cases reported in Figure 5 well describe the gen-

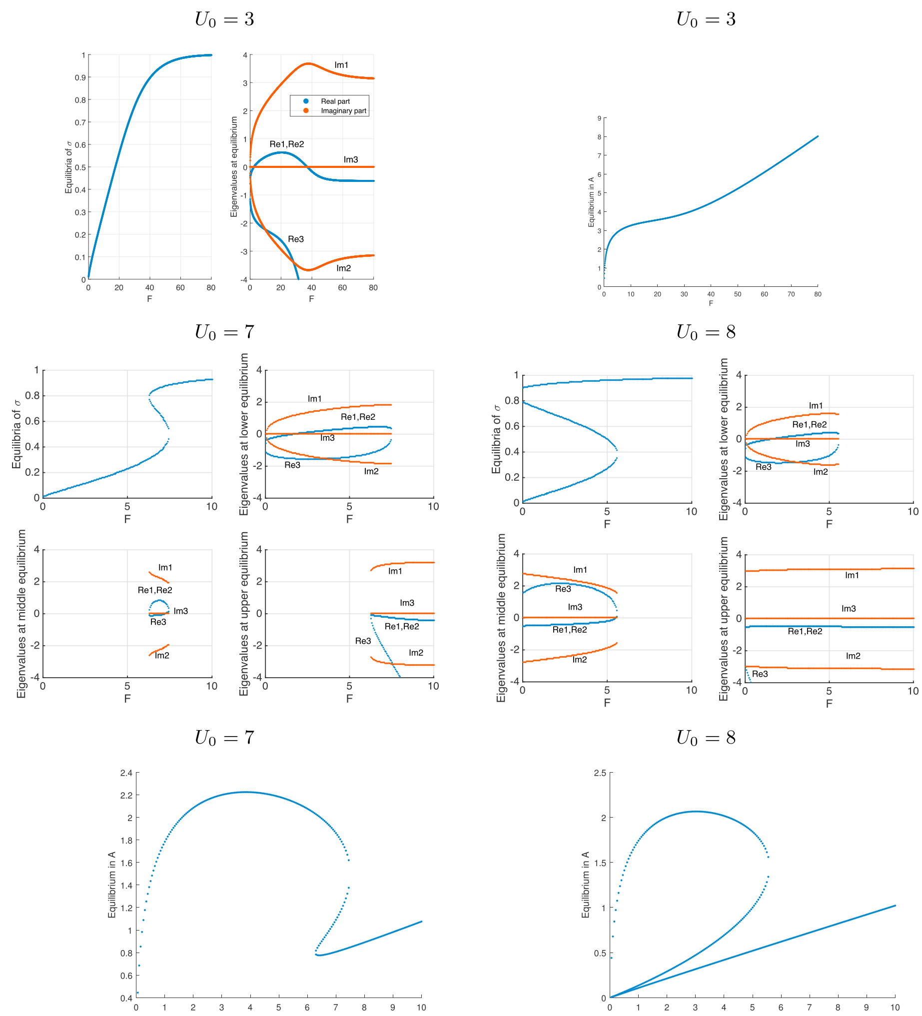

Figure 5. Equilibrium solutions and stability diagrams for the parameter regime in Table 1 when F is systematically varied from 0 to 10 and $U_0 = 3$ (top panels), $U_0 = 7$ (middle and bottom left panels), and $U_0 = 8$ (middle and bottom right panels). The equilibrium values of σ and A as well as the real (blue) and imaginary (red) parts of the eigenvalues of the associated Jacobian matrix are plotted against the values of F.

eral behavior of the system, which can be grossly summarized as follows. The system has either a single equilibrium or three equilibria. The lower equilibrium, when F is small enough, is stable; it then becomes a saddle node as F increases. If the system only has a single equilibrium throughout the entire range of F, the equilibrium becomes stable again as it approaches the upper limit $\sigma = 1$. If there are (as in the case with $U_0 = 8$) three equilibria for small F, the lower equilibrium may go from being stable to unstable before the bottom two equilibria disappear. Otherwise (as in the case $U_0 = 7$), it will be unstable by the time the two top equilibria appear. The middle equilibrium is always unstable (almost always a saddle node), and the upper equilibrium is always stable. The upper equilibrium, additionally, always has an eigenvector $[A, M, \sigma] \approx [0, 0, 1]$ with an eigenvalue with a large and negative real part. That is, the upper equilibrium tends to pull the solution toward the corresponding trivial solution very strongly.

In general, for small enough σ at equilibrium and small enough F, the system is stable. The system is also stable for large enough σ and large enough F. The system is unstable elsewhere. Moreover, we know that unstable modes appear in complex conjugate pairs owing to Hopf bifurcation with imaginary parts of the eigenvalues not exceeding a few units, as depicted in Figure 5, corresponding to oscillation periods of one to a few hours. This is consistent with the oscillation frequencies of the model with constant CAF reported in Figures 1-4, which themselves are consistent with the one cloud-type model akin to the results of Pan and Randall (1998).

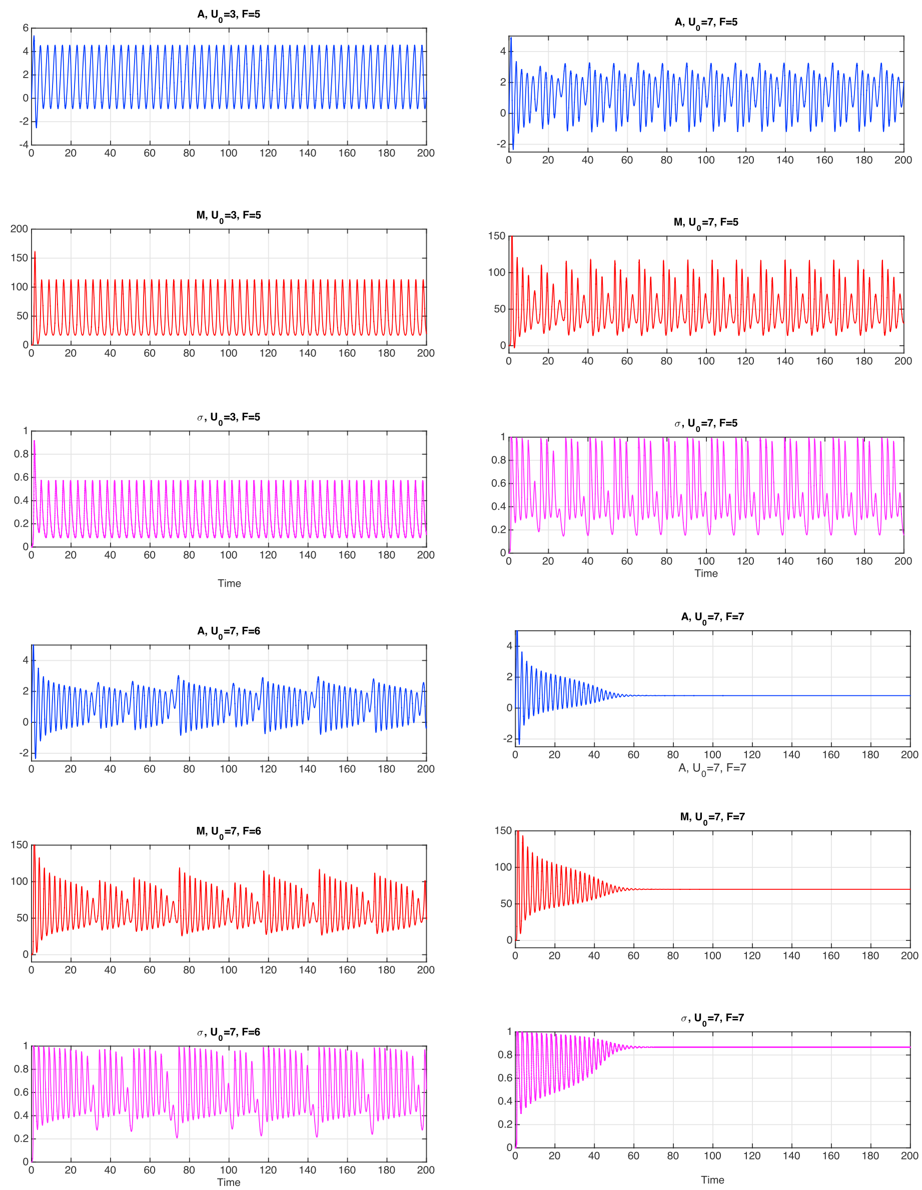

Figure 6. Solution time series for the cases of a single and unstable and multiple equilibria showcasing examples of simple limit cycle (top left) when $U_0 = 3$ and $F = 5$; chaotic behavior corresponding to $U_0 = 7, F = 5$ (top right), and $U_0 = 7, F = 6$ (bottom left); and damped oscillations (asymptotic spiral) for $U_0 = 7, F = 7$ (bottom right). Time unit is 1,000 s.

The equilibria with $\sigma \ll 1$ correspond to regimes of low cloud coverage that amount to states of scattered convection, while those with $\sigma \approx 1$ are associated with active convective organization and high cloud coverage. The results above suggest that the model preferentially predicts these two regimes as the two stable-limiting states, corresponding, respectively, to cases of weak and strong large-scale forcing, from the environmental meteorological variables. The intermediate regimes appear to be unstable thus non self-sustainable in the long run, independently on the strength of the environmental forcing. They may represent the successive transient states that exist between states of scattered convection and clear-sky regimes and those of fully organized convection.

We now numerically integrate the equations in (24) using an off-the-shelf Matlab$^{\text{TM}}$ routine (ODE23S) under the parameter regimes in Table 1 while focussing on some interesting cases revealed in Figure 5. The initial conditions are $A = M = \sigma = 0$. It is important to note at this point that while the discussion above focused mainly on the stability of the system, the eigenvalues always exhibited nonzero imaginary parts, especially those with positive real parts, corresponding to physical oscillations on the order of one to a few hours. We consider in particular the cases with a single and unstable equilibrium, corresponding to $U_0 = 3$ and $U_0 = 7$ when $F = 5$, a case of multiple equilibria represented by $U_0 = 7$ and $F = 6$, and a case of a single stable equilibrium associated with $U_0 = 7$ and $F = 7$. As illustrated by the solution time series plots in Figure 6, these four cases lead to a limit cycle, chaotic behavior, and damped oscillations, respectively. Only the last case portrays a damped oscillation behavior consistent with the single (uncoupled) cloud model with fixed CAF of Pan and Randall (1998). According to the dimensional units in (21), the periodic, chaotic, and damped oscillations in Figure 6, corresponding to the cases ($U_0 = 3, F = 5$), ($U_0 = 7, F = 5, 6$), and $U_0 = 7, F = 7$, respectively, have a nearly common period of about an hour or so with the chaotic cases exhibiting a multiscale behavior with a secondary longer period of about 5 hr. Such oscillations cannot be ignored or assumed to average out in a climate model simulation with a 10-min or even an hour time step.

3.2.2. Case of Variable Forcing

To mimic a somewhat more realistic situation, we consider the case when the forcing F oscillates between 0 and various upper values, driving the dynamical system across various bifurcation points, in the different parameter regimes discussed in Figure 5. Let T be the period of these oscillations. As before we integrate numerically the $M_b - A - \sigma$ system using Matlab$^{\text{TM}}$ with the trivial initial conditions $A = M_b = \sigma = 0$. We consider and compare various cases corresponding to different values of the parameter U_0 and various periods of the F oscillations, allowing us to compare cases when the system is driven either slowly or rapidly, between states of single equilibria, going either from small to large CAF coverage or from cases of stable to unstable equilibrium as well as cases when the system switches from states with a single equilibrium to states with multiple equilibria. More importantly, we compare cases when F oscillates slowly, relative to the system's internal modes, and cases when F oscillates more rapidly. Since F represents the environmental forcing in general, the forcing oscillations may occur on scales ranging from a few minutes to a few hours or even days due to multiple processes such as boundary layer turbulence, radiative forcing, and the diurnal cycle to name a few. Below, we consider cases with oscillation periods as small as 10 min as well as cases where the forcing period is close to one fifth of a day.

We begin with the case when $U_0 = 3$ and assume that F oscillates, as a sine wave, from 0 to to up to 50, both with a large period of $T = 20$ units, corresponding roughly to 5.5 hr according to (21), and a faster oscillation regime with a period $T = 0.6$ or 10 min. We note that, according to Figure 5, in the case of $T = 20$, except perhaps when F is near zero, there is a clear scale separation between the slow forcing and the cloud model that depicts frequencies, ω, ranging between 1 and 3.5 units (especially within the instability bubble), corresponding to periods, $2\pi/\omega$, ranging roughly between 2 and 6 units. When $T = 0.6$, the forcing oscillates much faster than the cloud model. These are two extreme limits that represent two separate physical situations. We note that only the case of slow F-oscillations is consistent with the QE assumption of Arakawa and Schubert (1974), while the second case is representative of much faster processes that may come from other components of the climate system such as turbulence and cloud microphysics. The latter can be alternatively captured by randomly induced noise, if, for example, the stochastic version (SMCM) of the CAF model in (15) is used instead (Khouider, 2014).

The solution time series corresponding to $U_0 = 3$ are plotted in Figure 7, starting with the cases when F oscillates between 0 and 50 with a period $T = 20$ and a period $T = 0.6$, which are shown on the top left and top right sets of panels, respectively. We see that somewhat consistent with the Pan and Randall model of damped oscillations, with the exception for having a variable CAF, in the first case the cloud model appears to follow the F-oscillations on average while it exhibits excursions from its varying equilibrium. These excursions are a manifestation of the system's own rapid oscillations as it switches back and forth between the lower equilibrium point of weak convection, when F is near zero, and the upper equilibrium point corresponding to large M_b and A values and a near saturation *CAF*. We note that in terms of A and σ the system spends more time near the upper equilibrium than it does near the near zero CAF point. Arguably, the sudden appearance of internal oscillations coincides with the instability bubble associated with the instances when $5 \leq F \leq 40$. However, only when the system transitions from the lower to the upper equilibrium these oscillations are seen; it comes down more rapidly and more smoothly as though the system experiences some sort of hysteresis. Notice also that, consistent with Figure 5, the CWF variable, A, oscillates between zero and around $A \approx 5$. However, in the case of rapid F oscillations, corresponding to $T = 0.6$, the solution appears to first undergo a transient period of roughly 15 time units, after which it oscillates with the forcing (with 16 oscillations per 10 time units). However, it does not follow the equilibrium

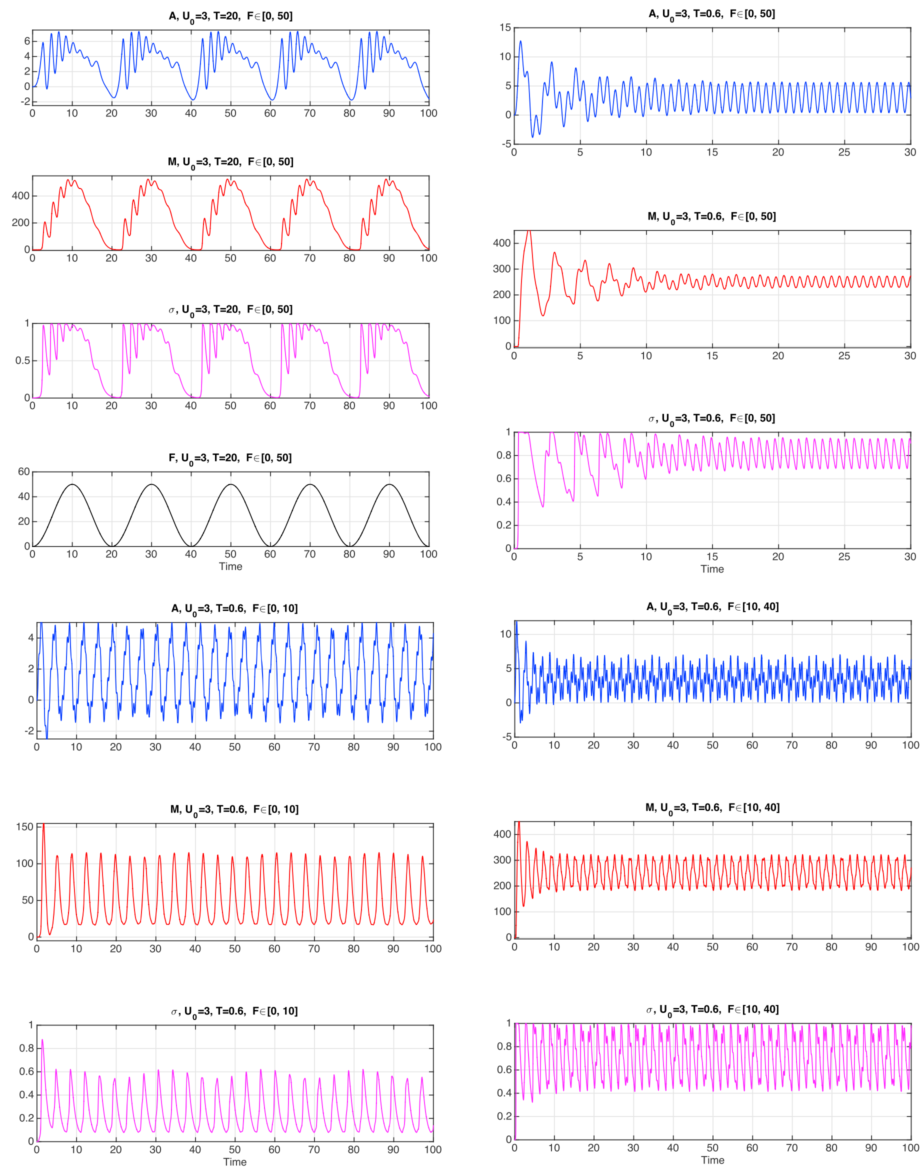

Figure 7. Solution time series for the A-M_b-σ-system when F varies. Case with $U_0 = 3$ and F oscillating between 0 and 50 with a period of 20 (top right), F oscillating between 0 and 50 with a period of 0.6 (top left), F oscillating between 0 and 10 with a period of 0.6 (bottom left), and F oscillating between 10 and 40 with a period of 0.6 (bottom left).

solution, as the cloud model does not have enough time to adjust, especially in terms of M_b and σ that appear to oscillate around intermediate values, far away from the extreme equilibria of the system, in clear violation of the QE theory.

On the bottom left and right panels of Figure 7, we set $U_0 = 3$ and $T = 0.6$, but the F values are now set to oscillate between 0 and 10 and between 10 and 40, respectively. According to Figure 5, in the first subcase, F drives the system from a stable equilibrium into the instability bubble and back, spending roughly the same amount of time in each regime, while in the second subcase it stays almost entirely within the instability bubble. Somewhat expectedly, in the first case the system enters some sort of a pseudo-limit cycle or strange attractor—akin to chaotic dynamical systems—with an oscillation (pseudo) period of roughly three, corresponding to a frequency $(2\pi/3)$ of roughy two units, which is within the range of those of the unstable modes, slightly beyond the bifurcation point at $F \approx 5$, as depicted in Figure 5. In the second case, the system depicts a slightly more complex behavior with two distinct scales of variability with the slower and more dominant one corresponding to a period of roughly two, consistent with the frequency associated with the

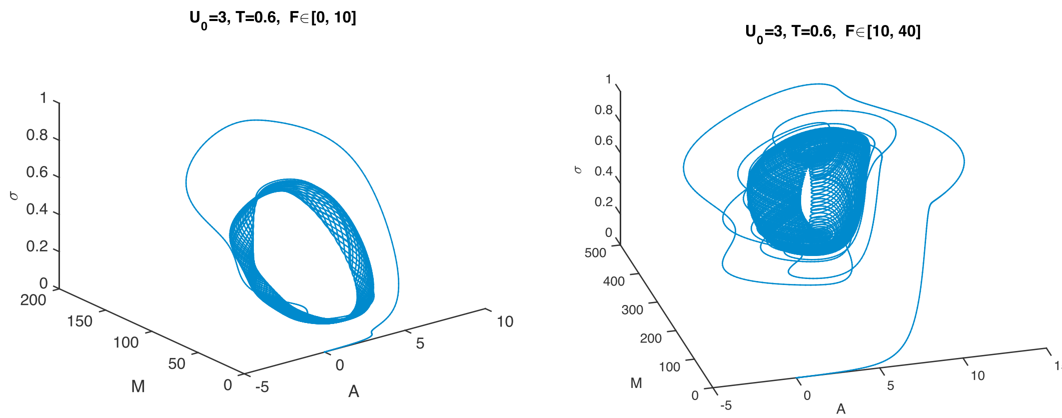

Figure 8. Longtime 3-D trajectories illustrating the strange attractors associated with the cases $U_0 = 3$, $T = 0.6$ and F varying between 0 and 10 (left) and between 10 and 40 (right) in Figure 7.

peak of instability reached around $F = 20$. Thus, the presence of the instability forces the system toward a pseudo-limit cycle or a strange attractor where it oscillates with the intrinsic frequency of the unstable mode. While the slow oscillations in F drive the solution back and forth between its stable equilibrium extremes, and the oscillatory behavior is manifested only during the transition from the lower to the upper equilibrium. When the F oscillations are fast, the system locks itself around a pseudo-limit cycle with multiscale oscillations. To confirm the emergence of a strange attractor, we plot in Figure 8 the 3-D trajectories, in the $M_b - A - \sigma$ space, of the longtime integrated solutions corresponding to last two cases, that is, $U_0 = 3$, $T = 0.6$ and F varying between 0 and 10 and between 10 and 40, respectively.

In Figure 9, we consider the case with $F_0 = 7$, where the forcing oscillations drive the system through bifurcations between single and multiple equilibria. First, we consider the case when F varies between 0 and 10, driving the system from a stable equilibrium with low CAF all the way to a state of a single equilibrium with high CAF, passing through regimes with a single stable equilibrium and regimes of multiple equilibria, where often only the high CAF one is stable. Three periods of F-oscillations, corresponding to a slow frequency case with $T = 20$, an intermediate case with $T = 4$ and a fast case with $T = 0.6$, are depicted in Figure 9, on the top-left, top-right, and bottom-left sets of panels, respectively. In the first case, we see a behavior that is consistent with the case of a single equilibrium in Figure 7 when $U_0 = 3$ as F tries to slowly drive the system between its equilibrium extremes while there is some internal resistance manifested by oscillations during the passage from the low to the high CAF states with somewhat longer oscillations.

When $T = 4$, the solution is phase locked with the forcing counterintuitively preventing resonance growth, perhaps due to a combination of nonlinear dynamics and the extreme stability of the equilibrium extremes near low and high CAF, respectively. With $T = 0.6$, however, the system exhibits nearly chaotic oscillations will a period of roughy three, coinciding roughly with the most unstable state of a single equilibrium near $F = 5$, which is also consistent with the case $U_0 = 3$ in Figure 7. On the bottom-right set of panels in Figure 9, F is set to vary on the same fast frequency at $T = 0.6$ but, with F values oscillating between 0 and 5, forcing the system to remain within the single equilibrium regime, according to Figure 5. However, because this equilibrium becomes unstable on the large side of F values, intermittent excursions toward high CAF values occur on a highly irregular basis. This, indeed, constitutes an intriguing counterexample of a very revealing behavior. Even if F itself does not drive the system to the upper equilibrium state, the instability of the lower equilibrium alone is capable of pushing the system toward it, providing an example of self-unresolved-scale-induced variability of the cloud model, which is clearly at odds with the QE theory. The 3-D trajectories corresponding to the last two cases are shown on the bottom panels of Figure 9. The emergence of a strangely shaped attractor is evident in both cases and the excursions to higher CAF state, which are less frequent in the case on the right are also evident.

In Figure 10, we consider the case with $U_0 = 8$, which, according to Figure 5, bifurcates from a state of multiple equilibria at low F to a state of a single, high CAF, equilibrium when $F \geq 5.5$ or so. On the top left panels, we consider the case of slow sine oscillations in F corresponding to $T = 20$, between 0 and 10, allowing in principle the passage through the two bifurcation points. However, as seen in Figure 10, while

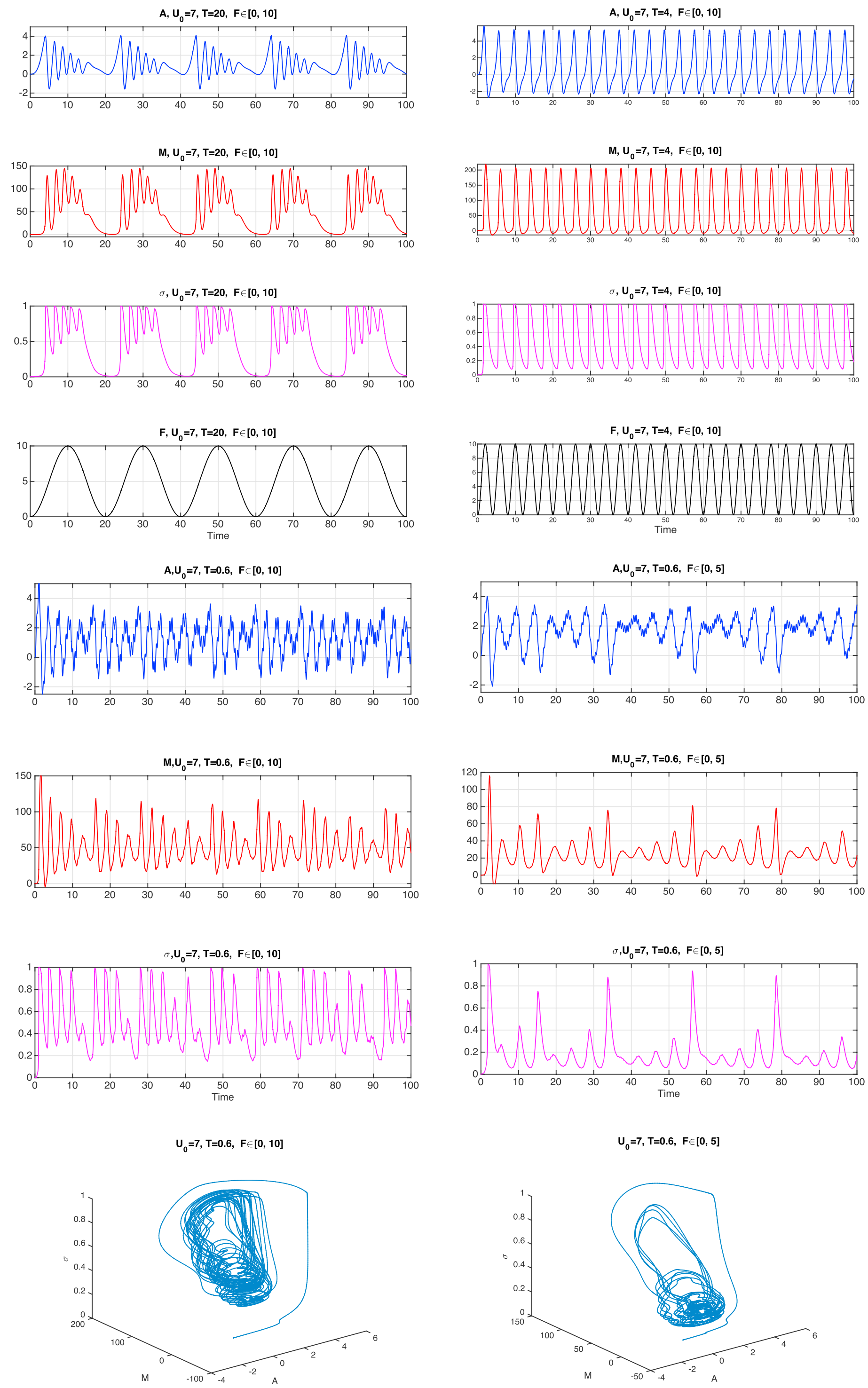

Figure 9. Same as Figure 7 but with $U_0 = 7$ and F varies between 0 and 10. Case when F oscillates with a long period of 20 (top left), a moderate period of 4 (top right), and rapid oscillation with a period of 0.6 (middle left). Also shown is a case when F oscillates between 0 and 5 with a period 0.6 (middle right). Bottom panels are 3-D trajectories for the chaotic solutions of the middle right and left panels, respectively.

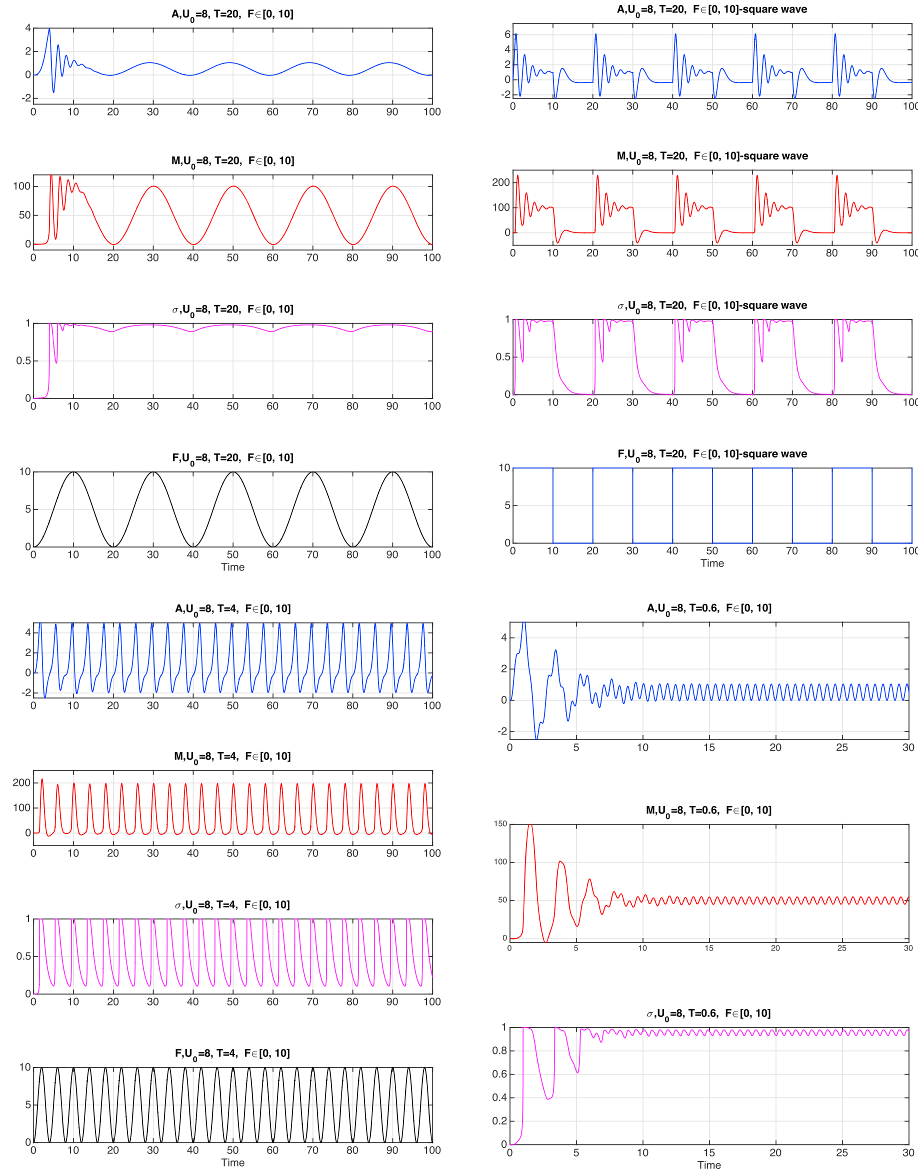

Figure 10. Same as Figure 7 but with $U_0 = 8$ and F varies between 0 and 10. Top left and top right panels are for period $T = 20$ when F is sine and a square wave, respectively. Bottom right and bottom left panels correspond to $T = 4$ and $T = 0.6$, respectively.

the solution seems to smoothly follow the forcing oscillations, it barely touches the lower equilibrium point when F hits 0, which constitutes yet another case and another way in which the QE assumption is violated even if there are not any rapid oscillations involved in neither the forcing nor the cloud-model response. Nonetheless, if F is set to oscillate as a square wave, the behavior on the top left panels in Figures 7 and 9 is reproduced. Somehow with the stronger internal interaction potential $U_0 = 8$, the smooth-sine oscillations do not provide enough residence time for the cloud model to reach the low CAF equilibrium state. In terms of the local interactions of the microscopic cloud model, the strong interactions with neighboring cells are capable of providing the resistance force needed to maintain the dynamical process at the upper equilibrium in that situation.

On the bottom two sets of panels in Figure 10, we consider the cases with $U_0 = 3$ when F oscillates between 0 and 10 with periods $T = 4$ and $T = 0.6$, respectively. In the first case, where the forcing period is comparable to the cloud model's internal oscillations, the solution phase locks with the forcing as in the case with $U_0 = 7$ on the top right of Figure 9, with strong oscillations switching back and forth between low and high CAF

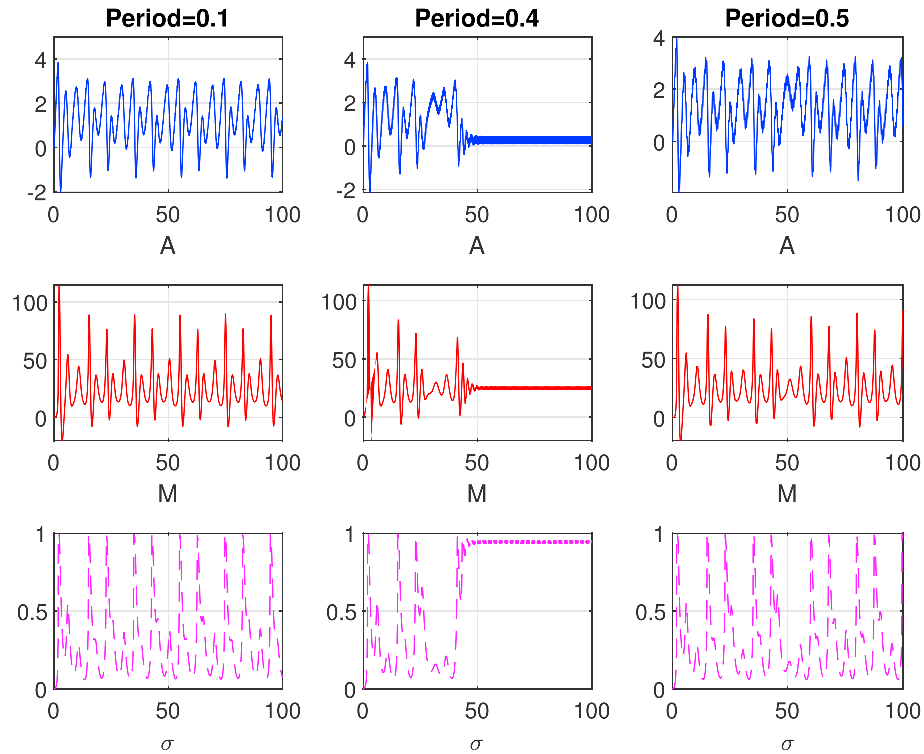

Figure 11. Same as Figure 7 but with $U_0 = 8$; F varies between 0 and 5 with periods 0.1,0.4, and 0.5.

values. In the second case, however, while in the long run the oscillation period is that of the forcing, the oscillation amplitudes are, as in the case with $T = 20$ on the top left panels, much less important, and the solution remains near the high CAF equilibrium. Note also a transient period of nearly 10, which is significantly less important than the one recorded for the case with $U_0 = 3$ on the top left panels of Figure 7. As it turns out, the behavior depicted in Figure 10 when $T = 0.6$ is very sensitive to T and the range of F oscillations. The solutions corresponding to three high frequency periods, corresponding to $T = 0.1$, $T = 0.4$ and $T = 0.5$, and F varying between 0 and 5 are shown in Figure 11. With F now spanning only the multiple equilibrium regime, according to Figure 5, chaotic behavior is seen in almost all three cases, at least during a significantly long transient period as for the case with $T = 0.4$ on the middle panels. We note that when the solution settles down to a regime of weak oscillations, it does so near the high CAF equilibrium point, which is again inconsistent with the QE theory, which is based on an always-fixed low CAF hypothesis.

4. Discussion and Concluding Remarks

Since its introduction, the QE theory of cumulus convection parameterization (Arakawa & Schubert, 1974), has been the subject of many studies (Bechtold et al., 2014; Emanuel & Raymond, 1993; Lin et al., 2015; Lord & Arakawa, 1980; Lord, 1982; Neelin & Zeng, 2000; Pan & Randall, 1998; Raymond & Herman, 2011). While most of the early work was to validate or justify the QE hypothesis using data, a few works have been devoted to alternatives for the convection parameterization problem. Inspired by Pan and Randall (1998), the presented work is a proposal route toward a closure for mass-flux cumulus schemes based on a stochastic model for the CAF, namely, the SMCM of Khouider et al. (2010). By closing the budget equations for the CWF and CKE through a cloud base mass-flux-kinetic energy relationship, Pan and Randall (1998) derived a prognostic model as an alternative for the strict QE closure. By assuming that the main action of cumulus activity is to reduce the CWF, which amounts to ignoring the cloud-cloud interactions, Pan and Randall demonstrated that the prognostic closure model undergoes damped oscillations on the order of the CKE dissipation timescale. This timescale is comparable to the time it takes for deep cumulonimbus clouds to form stratiform anvils, for example, and as such the prognostic closure provides the missing memory for the cumulus scheme, which is needed to overcome some of the known shortcomings of the QE theory.

Here, we took a few steps forward in the same direction. First, we demonstrate that if cloud-cloud interactions are taking into account, the CKE-CWF equations can become unstable, and important bifurcations occur when key model parameters are varied. Specifically, we assume that the interaction kernel is a constant coefficient matrix with positive entries below the diagonal and negative entries elsewhere, so that the CWF for a given cloud type is increased by shallower cloud types and decreased by all other cloud types, consistent with the intuition that shallow cumulus and cumulus congestus moisten and precondition the environment for deep cumulonimbus (Arakawa & Schubert, 1974; Johnson et al., 1999). We considered, separately, the cases of interacting two and three clouds, representing, for example, shallow and deep cloud types and shallow, congestus, and deep cloud types, respectively. We found that the CWF-CKE system with multiple cloud types leads to damped oscillations as in the Pan and Randall model, but only when the diagonal elements of the kernel matrix are dominant or when the CAF of one of the cloud types dominates. In all other cases, growing modes emerge, making the prognostic closure equations unstable, which is at odds with the QE theory and further enforces the need for a prognostic closure.

Second, and more importantly, we proposed a substantial refinement for the Pan and Randall prognostic closure model using the mean field limit of the extended SMCM with nearest neighbor interactions of Khouider (2014) to provide complementary dynamical equations for the distinct cloud-type area fractions (CAF), σ_λ. The case of a single cloud is thoroughly analyzed. The resulting CWF-CKE-CAF equations are highly nonlinear, and as such they possess rich dynamics including multiple equilibria, limit cycles, and chaotic dynamics. We showed that the coupled system sometimes has a single equilibrium and sometimes it has multiple equilibria, depending of the strength of the internal-local interaction potential of the SMCM, U_0. Also, depending on the strength of the large-scale forcing, F, akin to the environmental variables, the equilibria can be stable or unstable. The multiple equilibria always appear in triads and are classified according to their CAF values: a lower equilibrium associated with the lowest CAF value, an upper equilibrium corresponding to the highest CAF value, and a middle equilibrium corresponding to the intermediate CAF value. The middle equilibrium is always unstable, a saddle node, and the upper equilibrium is always stable. The lower equilibrium is stable for small values of F and becomes unstable as F is increased.

As demonstrated in Figure 5, with $U_0 = 3$, small values of U_0 lead to a single equilibrium independently of F, which is stable and has small CAF, with a value $\sigma \approx 0$, when F is small and stable with high CAF, with a value $\sigma \approx 1$, when F is large. For intermediate values of F, the equilibrium with intermediate CAF values is unstable. Multiple equilibria emerge at higher values of U_0 and for either intermediate values of F and moderate U_0 or small values of F and sufficiently large U_0, as illustrated in Figure 5, in the cases of $U_0 = 7$ and $U_0 = 8$, respectively. Independently of U_0, if F is large enough, there is only one equilibrium point, and it coincides with a high CAF coverage near $\sigma = 1$. The equilibrium point with $\sigma \approx 1$ coincides with the point of minimum energy that maximizes the Gibbs measure in (12). This may explain in part its unconditional stability. The lower equilibrium on the other hand is associated with the highest energy equilibrium and appears to be easily destabilized by the large-scale forcing, while the middle equilibrium is unstable by the nature of the particle interacting system (Khouider & Bihlo, 2018; Majda & Khouider, 2002).

Independently of the strength of the local interactions, the CWF-CKE-CAF system is capable of producing interesting dynamics that clearly demonstrate the limitation of the QE theory. As shown in Figure 6, even in the case with constant forcing, we can have situations of a purely periodic solution (limit cycle), chaotic behavior, or damped oscillations. While all these examples are in line with Pan and Randall's seminal work of providing grounds for deriving and justifying the use of prognostic closure equations for the cloud base mass flux, only the last example is consistent with their assumption of holding CAF fixed and making the CWF kernel to only damp CWF.

The existence of chaotic dynamics and periodic solutions clearly warrants against the use of a single-fixed CAF value. This point is further demonstrated by the examples with varying forcing illustrated in Figures 7–11. The case of weak internal interactions in Figure 7, for example, demonstrates that when F is slowly driving the cloud model relative to the system's internal frequencies, the time integrated solution adjusts to the forcing in the long run, but with significant resistance manifested by rapid and large amplitude oscillations. This in particular occurs when the CAF is driven upward from near $\sigma = 0$ to near $\sigma = 1$; the solution comes back down more slowly and smoothly, suesting some form of hysteresis. The resistant oscillations become much stronger when the interaction potential is increased to $U_0 = 7$. At $U_0 = 8$, the case of slowly oscillating forcing locks the area fraction near the upper equilibrium because it is the most stable and most prevailing equilibrium in this case. Though the associated high CAF value is at odds with the small CAF value assumption, this is perhaps the only example that somewhat justifies a QE approximation. However, the argument breaks down if F is set to vary as a square wave instead of a sine wave as illustrated on the top right panels of Figure 10. Such rapid switching in the forcing, exemplified by the square wave, is ubiquitous in the phenomenon of convection because, by nature, convection is associated with sudden release of a large-scale instability.

When the forcing is made to oscillate on frequencies that are comparable to those of the cloud model, the solution appears to synchronize nicely with the forcing without apparent resonance growth, perhaps because of the strong stability of the equilibria at the extreme limits associated with zero CAF and full coverage CAF, respectively. Nonetheless, the oscillating solution deviates significantly from the equilibrium as it switches back and forth from the lower and upper CAF limits in a highly asymmetric fashion.

When the forcing is made to oscillate faster then the internal modes of the system, the solution often becomes chaotic again as in the case of a constant forcing, especially when the forcing is made to span both stable and unstable parts of the bifurcation diagram. However, this behavior is not at all universal, as illustrated by the case of strong local interactions on the bottom right of Figure 10, where the solution appears to settle to regular but weak oscillations near the upper equilibrium though after a significant chaotic transient period of nearly 10 units of time corresponding to nearly 3 hr, consistent with the damped oscillations of Pan and Randall (1998). However, the further tests reported in Figure 11 demonstrate that slightly changing the period of the forcing leads to highly significant extension of the transient period. Also, tests not reported here show that when the $M_b - A - \sigma$ equations in (24) are modified so that positive only M_b is allowed to feedback onto the CWF equation, by replacing M_b by $\max(M_b, 0)$, the same mere extension of the chaotic transient period is observed.

Similarly to the square wave example, the rapid oscillations in the large-scale forcing can be symptomatic of rapid variations in the large-scale state variables due to turbulence or cloud microphysics, especially for climate and weather prediction models that are run at high resolution, within the so-called gray zone (Buizza et al., 1999; Grell & Devenyi, 2002; Sun et al., 2014). When not present, such oscillations can be emulated by the use of the stochastic version of the SMCM instead of the mean field equations in (15) (Khouider, 2014).

The work presented here demonstrates that a prognostic closure that couples the CKE-CWF equations of Pan and Randall (1998) to the SMCM of Khouider (2014) for CAF will provide a better representation of the deviations of convection from QE, potentially improve the performance of climate and weather prediction models especially at high resolution, and allow (parametrized) convection to self-organize on multiple temporal and spatial scales in an intermittent and chaotic fashion. The CKE-CWF-CAF can in particular represent and capture the effect of organized convection on multiple scales including convective mesoscale systems and squall lines that occur on subgrid scale in coarse-resolution GCMs. Both local and nonlocal external effects such as vertical shear, orography, land-sea contrast in addition to other common predictors such as CAPE, CIN, and midlevel moisture can be used in place of the external and local interaction potentials h and U in (13). The local interaction potential can be easily modified to allow asymmetries to vertical, topography, or land-sea contrast, for example, to allow self-organization and propagation of mesoscale systems (Bergemann et al., 2017; Khouider & Moncrieff, 2015). This idea will be pursued and tested by the authors, in the near future for the case of a single column atmospheric model, and the results will be reported elsewhere.

Appendix A: Nondimensionalization of the CKE-CWF System

Let $\hat{A}$, $\hat{M}$, $\hat{J}$, $\hat{\alpha}$, $\hat{F}$, $\hat{t}$, and $\hat{\tau}$ be the reference dimensional units of the CWF, the cloud base mass flux, the cloud kernel, the forcing, time, the cloud-base mass flux-CKE proportionality constant, and the dissipation timescale, respectively. The CKE-CWF system can be represented as

$$\frac{\hat{A}}{\hat{t}}\frac{dA_\lambda}{dt} = \hat{J}\hat{M}(K * M_{b,\lambda})_\lambda + \hat{F}F_\lambda,$$

$$\frac{\hat{M}}{\hat{t}}\frac{dM_\lambda}{dt} = \frac{\hat{A}}{\hat{\alpha}}\beta_\lambda A_\lambda + \frac{\hat{M}}{\hat{\tau}}\frac{1}{\tau}M_{b,\lambda},$$

with the variables without hats being dimensionless and of order 1.

Bringing all the hats over to one side, we get

$$\frac{dA_\lambda}{dt} = J_0(J * M_{b,\lambda})_\lambda + F_0 F_\lambda,$$

$$\frac{dM_\lambda}{dt} = A_0 \beta_\lambda A_\lambda + \frac{1}{\tau_0}\frac{1}{\tau} M_{b,\lambda},$$

where $J_0 = \frac{\hat{J}\hat{M}\hat{t}}{\hat{A}}$, $F_0 = \frac{\hat{F}\hat{t}}{\hat{A}}$, $A_0 = \frac{\hat{A}\hat{t}}{\hat{\alpha}\hat{M}}$, and $\tau_0 = \frac{\hat{\tau}}{\hat{t}}$.

It remains to find the approximate values of the hatted variables. We can assume from Arakawa and Schubert (1974) that $\frac{dA_\lambda}{dt}$ is approximately bounded above and below by $\pm 0.08 \text{cal} \cdot \text{g}^{-1} \cdot \text{day}^{-1} \approx \pm 0.004 \text{J} \cdot \text{kg}^{-1} \cdot \text{s}^{-1}$.

Since pressure can be assumed to be bounded between 150 and 800 mb, we can assume, from Lord (1982), that the mean forcing over the period of a day is bounded between 0.15 to 2.0 $\text{kJ} \cdot \text{kg}^{-1} \cdot \text{day}^{-1}$ ($\approx$0.04 to $0.55 \text{J} \cdot \text{kg}^{-1} \cdot \text{s}^{-1}$).

From the same paper, assuming that pressure is approximately 800 mb at cloud base, we assume that the time-averaged base mass flux (in terms of pressure, gM_b) is bounded by 0.1 and 0.7 mb/hr ($\approx$ 0.0028, 0.019$\text{N} \cdot \text{m}^{-2} \cdot \text{s}^{-1}$). From the fact that $g \approx 10$ m/s^2, the base mass flux in terms of height is approximately bounded by 0.00028 and 0.0019 $(\text{N} \cdot \text{m}^{-2} \cdot \text{s}^{-1})(\text{m}^{-1} \cdot \text{s}^2) = \text{kg} \cdot \text{m}^{-2} \cdot \text{s}^{-1}$.

We can reasonably assume, from the formula for A, that it is approximately 300 m^2/s^2. Since $\frac{dA_\lambda}{dt} - F_\lambda = (K * M)_\lambda$, $(K * M)_\lambda$ is bounded above by $0.004 - 0.04 = -0.036$ and below by $-0.004 - 0.055 \approx -0.06$. Since $(K * M)_\lambda$ is actually a summation of terms, it is impossible to find an exact bound for M_λ, but we know that M_λ is somewhere on the order of magnitudes 10^{-3} and 10^{-4}, and $(K * M)_\lambda$ on the order of magnitude of 10^{-2}. Thus, we can say elements J of K are somewhere on the order of magnitudes of 10^1 and 10^2 $\text{m}^4 \cdot \text{kg}^{-1} \cdot \text{s}^{-2}$.

From Pan and Randall (1998), we can assume that $\frac{\sigma_\lambda}{2\alpha_\lambda}$ is between 10^{-7} and 10^{-9} m^4/kg and that τ_λ is between 600 and 1,200 s.

To summarize that which we have so far,

$$\begin{aligned} \left[\frac{dA_\lambda}{dt}\right] &\sim \pm 4 \cdot 10^{-3} \frac{\text{J}}{\text{kg s}} \\ \left[F_\lambda\right] &\sim 4 \cdot 10^{-2} - 5.5 \cdot 10^{-1} \frac{\text{J}}{\text{kg s}} \end{aligned},$$

$$\begin{aligned} \left[M_{b,\lambda}\right] &\sim 2.8 \cdot 10^{-4} - 2 \cdot 10^{-3} \frac{\text{kg}}{\text{s m}^2} \\ \left[\frac{\sigma_\lambda}{2\alpha_\lambda}\right] &\sim 10^{-8} \frac{\text{kg}}{\text{m}^4} \\ [\tau] &\sim 600 - 1,200\text{s}. \end{aligned}.$$

Since $\frac{dA}{dt} \ll F$, we assume that $[JM_\lambda] \sim [F_\lambda]$, so that

$$[J] \sim \frac{4 \cdot 10^{-2} - 5.5 \cdot 10^{-1}}{2.8 \cdot 10^{-5} - 2 \cdot 10^{-3}} \frac{\text{J kg}^{-1} \ \text{s}^{-1}}{\text{kg m}^{-2} \ \text{s}^{-1}} = 20 - 2,000 \frac{\text{m}^4}{\text{kg s}^2}.$$

We also assume, for the moment without justification, that $[\beta_\lambda A] \sim \left[\frac{M_\lambda}{\tau_\lambda}\right]$, so that

$$[A] \sim \frac{2.8 \cdot 10^{-4} - 2 \cdot 10^{-3} \ \text{kg s}^{-1} \ \text{m}^{-2}}{1000 \ \text{s} \cdot 10^{-8} \ \text{kg m}^{-4}} = 28 - 200 \frac{\text{m}^2}{\text{s}^2}.$$

This is supported by Lord and Arakawa (1980).

Thus, to make the hatless variables in the system (1) have order of magnitude 1, pick $\hat{J} = 100 \frac{\text{m}^4}{\text{kg s}^2}$, $\hat{M} = 10^{-3} \frac{\text{kg}}{\text{m}^2 \ \text{s}}$, $\hat{\alpha} = 10^8 \frac{\text{m}^4}{\text{kg}}$, $\hat{\tau} = \hat{t}$ =1,000s, $\hat{A} = 10^2 \frac{\text{m}^2}{\text{s}^2}$.

Then J_0, F_0, A_0, and τ_0 are all 1, and thus, system (1) is

$$\frac{dA_\lambda}{dt} = (K * M_{b,\lambda})_\lambda + F_\lambda \frac{dM_\lambda}{dt} = \beta A_\lambda + \frac{1}{\tau} M_{b,\lambda},$$

where K, F_λ, β, and τ have order of magnitude 1. This means that A and M vary on the same timescale.

Acknowledgments
The research of B. K. is partially funded by a grant from the Natural Sciences and Engineering Research Council of Canada (NSERC). This research was conducted in the context of E. L.'s NSERC Undergraduate Student Research Award. No new data has been used during this research. We are grateful to Mitch Moncrieff and the two other anonymous referees for their thoughtful comments and suggestions that greatly helped improve this paper from its original submission.

References

Arakawa, A. (2004). The cumulus parameterization problem: Past, present, and future. *Journal of Climate*, *17*(13), 2493–2525. https://doi.org/10.1175/1520-0442(2004)017<2493:RATCPP>2.0.CO;2

Arakawa, A., & Schubert, W. H. (1974). Interaction of a cumulus cloud ensemble with large-scale environment, Part I. *Journal of the Atmospheric Sciences*, *31*(3), 674–701.

Arakawa, A., & Wu, C. M. (2013). A unified representation of deep moist convection in numerical modeling of the atmosphere. Part I. *Journal of the Atmospheric Sciences*, *70*(7), 1977–1992. https://doi.org/10.1175/JAS-D-12-0330.1

Bechtold, P., Semane, N., Lopez, P., Chaboureau, J. P., Beljaars, A., & Bormann, N. (2014). Representing equilibrium and nonequilibrium convection in large-scale models. *Journal of the Atmospheric Sciences*, *71*(2), 734–753. https://doi.org/10.1175/JAS-D-13-0163.1

Bergemann, M., Khouider, B., & Jakob, C. (2017). Coastal tropical convection in a stochastic modeling framework. *Journal of Advances in Modeling Earth Systems*, *9*, 2561–2582. https://doi.org/10.1002/2017MS001048

Berner, J., Achatz, U., Batté, L., Bengtsson, L., CáMara, A. D. L., Christensen, H. M., & Yano, J. I. (2016). Stochastic parameterization: Towards a new view of weather and climate models. *Bulletin of the American Meteorological Society*, *98*(3), 3–7. https://doi.org/10.1175/BAMS-D-15-00268.1

Betts, A. K. (1986). A new convective adjustment scheme. Part I: Observational and theoretical basis. *Quarterly Journal of the Royal Meteorological Society*, *112*, 677–692.

Betts, A. K., & Miller, M. J. (1986). A new convective adjustment scheme. Part II: Single column tests using GATE wave, BOMEX, atex and arctic air-mass data sets. *Quarterly Journal of the Royal Meteorological Society*, *112*(473), 693–709.

Bretherton, C. S., & Park, S. (2008). A new bulk shallow-cumulus model and implications for penetrative entrainment feedback on updraft buoyancy. *Journal of the Atmospheric Sciences*, *65*(7), 2174–2193. https://doi.org/10.1175/2007JAS2242.1

Buizza, R., Miller, M., & Palmer, T. N. (1999). Stochastic representation of model uncertainties in the ECMWF ensemble prediction system. *Quarterly Journal of the Royal Meteorological Society*, *125*, 2887–2908.

Cardoso-Bihlo, E., Khouider, B., Schumacher, C., & Chevrotière, M. D. L. (2019). Using radar data to calibrate a stochastic parametrization of organized convection. *Journal of Advances in Modeling Earth Systems accepted*. https://doi.org/10.1029/2018MS001537

Charney, J. G., & Eliassen, A. (1964). On the growth of the hurricane depression. *Journal of the Atmospheric Sciences*, *21*, 68–75.

Deng, Q., Khouider, B., & Majda, A. J. (2015). The MJO in a coarse-resolution GCM with a stochastic multicloud parameterization. *Journal of the Atmospheric Sciences*, *72*(1), 55–74. https://doi.org/10.1175/JAS-D-14-0120.1

Derbyshire, S. H., Beau, I., Bechtold, P., Grandpeix, J. Y., Piriou, J. M., Redelsperger, J. L., & Soares, P. M. M. (2004). Sensitivity of moist convection to environmental humidity. *Quarterly Journal of the Royal Meteorological Society*, *130*, 3055–3080.

Dorrestijn, J., Crommelin, D., Biello, J., & Boing, S. (2013). A data-driven multicloud model for stochastic parameterization of deep convection. *Philosophical Transactions of the Royal Society A*, *371*, 1–19. https://doi.org/10.1098/rsta.2012.0374

Dorrestijn, J., Crommelin, D. T., Siebesma, A. P., Jonker, H. J., & Selten, F. (2016). Stochastic convection parameterization with Markov chains in an intermediate-complexity GCM. *Journal of the Atmospheric Sciences*, *73*(3), 1367–1382.

Emanuel, K. A., & Raymond, D. J. (1993). The representation of cumulus convection in numerical models. *Meteorological Monographs*, *46*, 1–246. https://doi.org/10.1175/0065-9401-24.46.1

Frenkel, Y., Majda, A. J., & Khouider, B. (2012). Using the stochastic multicloud model to improve tropical convective parameterization: A paradigm example. *Journal of the Atmospheric Sciences*, *69*, 1080–1105.

Ganai, M., Krishna, R. P. M., Mukhopadhyay, P., & Mahakur, M. (2016). The impact of revised simplified Arakawa-Schubert scheme on the simulation of mean and diurnal variability associated with active and break phases of indian summer monsoon using CFSV2. *Journal of Geophysical Research: Atmospheres*, *121*, 9301–9323. https://doi.org/10.1002/2016JD025393

Goswami, B. B., Khouider, B., Phani, R., Mukhopadhyay, P., & Majda, A. J. (2017a). Improved tropical modes of variability in the NCEP Climate Forecast System (Version 2) via a stochastic multicloud model. *Journal of the Atmospheric Sciences*, *74*(10), 3339–3366. https://doi.org/10.1175/JAS-D-17-0113.1

Goswami, B. B., Khouider, B., Phani, R., Mukhopadhyay, P., & Majda, A. J. (2017b). Improving synoptic and intraseasonal variability in CFSV2 via stochastic representation of organized convection. *Geophysical Research Letters*, *44*, 1104–1113. https://doi.org/10.1002/2016GL071542

Grabowski, W. W. (2004). An improved framework for superparameterization. *Journal of the Atmospheric Sciences*, *61*, 1940–1952.

Grell, G. A., & Devenyi, D. (2002). A generalized approach to parameterizing convection combining ensemble and data assimilation techniques. *Geophysical Research Letters*, *29*(14), 1693. https://doi.org/10.1029/2002GL015311

Grell, G. A., & Freitas, S. R. (2014). A scale and aerosol aware stochastic convective parameterization for weather and air quality modeling. *Atmospheric Chemistry and Physics*, *14*(10), 5233–5250. https://doi.org/10.5194/acp-14-5233-2014

Grell, G. A., Kuo, Y. H., & Pasch, R. J. (1991). Semiprognostic tests of cumulus parameterization schemes in the middle latitudes. *Monthly Weather Review*, *119*(1), 5–31. https://doi.org/10.1175/1520-0493(1991)119<0005:STOCPS>2.0.CO;2

Hohenegger, C., & Stevens, B. (2013). Preconditioning deep convection with cumulus congestus. *Journal of the Atmospheric Sciences*, *70*(2), 448–464.

Hung, M. P., Lin, J. L., Wang, W., Kim, D., Shinoda, T., & Weaver, S. J. (2013). MJO and convectively coupled equatorial waves simulated by CMIP5 climate models. *Journal of Climate*, *26*(17), 6185–6214. https://doi.org/10.1175/JCLI-D-12-00541.1

Jiang, X., Waliser, D. E., Xavier, P. K., Petch, J., Klingaman, N. P., Woolnough, S. J., & Zhu, H. (2015). Vertical structure and physical processes of the Madden-Julian oscillation: Exploring key model physics in climate simulations. *Journal of Geophysical Research:Atmospheres*, *120*, 4718–4748. https://doi.org/10.1002/2014JD022375

Johnson, R. H., Ciesielski, P. E., Ruppert, J. H., & Katsumata, M. (2015). Sounding-based thermodynamic budgets for dynamo. *Journal of the Atmospheric Sciences*, *72*(2), 598–622. https://doi.org/10.1175/JAS-D-14-0202.1

Johnson, R. H., Rickenbach, T. M., Rutledge, S. A., Ciesielski, P. E., & Schubert, W. H. (1999). Trimodal characteristics of tropical convection. *Journal of Climate*, *12*(8), 2397–2418.

Kain, J. S., & Fritsch, J. M. (1990). A one-dimensional entraining/detraining plume model and its application in convective parameterization. *Journal of the Atmospheric Sciences*, *47*(23), 2784–2802.

Kao, C. Y. J., & Ogura, Y. (1987). Response of cumulus clouds to large-scale forcing using the Arakawa-Schubert cumulus parameterization. *Journal of the Atmospheric Sciences*, *44*(17), 2437–2458. https://doi.org/10.1175/1520-0469(1987)044<2437:ROCCTL>2.0.CO;2

Khairoutdinov, M., Randall, D., & Demott, C. (2005). Simulations of the atmospheric general circulation using a cloud-resolving model as a superparameterization of physical processes. *Journal of the Atmospheric Sciences*, *62*, 2136–2154.

Khouider, B. (2014). A coarse grained stochastic multi-type particle interacting model for tropical convection: Nearest neighbour interactions. *Communications in Mathematical Sciences*, *12*, 1379–1407.

Khouider, B., Biello, J., & Majda, A. J. (2010). A stochastic multicloud model for tropical convection. *Communications in Mathematical Sciences*, *8*(1), 187–216.

Khouider, B., & Bihlo, A. (2018). A new stochastic model for the boundary layer clouds and stratocumulus phase transition regimes: Open cells, closed cells, and convective rolls. *Journal of Geophysical Research: Atmospheres*, *124*, 367–386. https://doi.org/10.1029/2018JD029518

Khouider, B., & Majda, A. J. (2006). A simple multicloud parameterization for convectively coupled tropical waves. Part I: Linear analysis. *Journal of the Atmospheric Sciences*, *63*, 1308–1323.

Khouider, B., Majda, A. J., & Stechmann, S. N. (2013). Climate science in the tropics: Waves, vortices and PDEs. *Nonlinearity*, *26*(1), R1–R68.

Khouider, B., & Moncrieff, M. W. (2015). Organized convection parameterization for the ITCZ. *Journal of the Atmospheric Sciences*, *72*(8), 3073–3096. https://doi.org/10.1175/JAS-D-15-0006.1

Kim, D., & Kang, I. S. (2012). A bulk mass flux convection scheme for climate model: Description and moisture sensitivity. *Climate Dynamics*, *38*, 411–429. https://doi.org/https://doi.org/10.1007/s00382-010-0972-2

Kim, D., Sperber, K., Stern, W., Waliser, D., Kang, I. S., Maloney, E., & Zhang, G. (2009). Application of MJO simulation diagnostics to climate models. *Journal of Climate*, *22*, 6413–6436.

Kuo, H. L. (1965). On formation and intensification of tropical cyclones through latent heat release by cumulus convection. *Journal of the Atmospheric*, *22*, 40–63.

Kuo, H. L. (1974). Further studies of the parameterization of the influence of cumulus convection on large-scale flow. *Journal of the Atmospheric Sciences*, *31*(5), 1232–1240.

Liggett, T. (1999).

Lin, J. L., Kiladis, G. N., Mapes, B. E., Weickmann, K. M., Sperber, K. R., Lin, W., & Scinocca, J. F. (2006). Tropical intraseasonal variability in 14 IPCC AR4 climate models Part I: Convective signals. *Journal of Climate*, *19*, 2665–2690.

Lin, J., Lee, M., Kim, D., Kang, I., & Frierson, D. (2008). The impacts of convective parameterization and moisture triggering on AGCM-simulated convectively coupled equatorial waves. *Journal of Climate*, *21*(5), 883–909.

Lin, J., & Neelin, J. D. (2000). Influence of a stochastic moist convective parameterization on tropical climate variability. *Geophysical Research Letters*, *27*, 3691–3694.

Lin, J. L., Qian, T., Shinoda, T., & Li, S. (2015). Is the tropical atmosphere in convective quasi-equilibrium? *Journal of Climate*, *28*, 4357–4372. https://doi.org/10.1175/JCLI-D-14-00681.1

Lord, S. J. (1982). Interaction of a cumulus cloud ensemble with the large-scale environment. Part III: Semi-prognostic test of the Arakawa-Schubert cumulus parameterization. *Journal of the Atmospheric Sciences*, *39*(1), 88–103. https://doi.org/10.1175/1520-0469(1982)039<0088:IOACCE>2.0.CO;2

Lord, S. J., & Arakawa, A. (1980). Interaction of a cumulus cloud ensemble with the large-scale environment. Part II. *Journal of the Atmospheric Sciences*, *37*(12), 2677–2692. https://doi.org/10.1175/1520-0469(1980)037<2677:IOACCE>2.0.CO;2

Majda, A. J. (2007). Multiscale models with moisture and systematic strategies for superparameterization. *Journal of the Atmospheric Sciences*, *64*, 2726–2734.

Majda, A. J., & Khouider, B. (2002). Stochastic and mesoscopic models for tropical convection. *Proceedings of the National Academy of Sciences of the United States of America*, *99*, 1123–1128.

Manabe, S., Smagorinsky, J., & Strickler, R. F. (1965). Simulated climatology of a general circulation model with a hydrologic cycle. *Monthly Weather Review*, *93*(12), 769–798.

Mapes, B. E., & Neale, R. B. (2011). Parameterizing convective organization to escape the entrainment dilemma. *Journal of Advances in Modeling Earth Systems*, *3*, M06004. https://doi.org/10.1029/2011MS000042

Meehl, G. A., Stocker, T., Collins, W., Friedlingstein, P., Gaye, A., Gregory, J. M., & Zhao, Z. (2007). Cambridge University Press, Cambridge, UK and New York, NY, USA. http://www.ipcc.ch/ipccreports/ar4-wg1.htm

Moncrieff, M. W. (1992). Organized convective systems: Archetypal dynamical models, mass and momentum flux theory, and parameterization. *Quarterly Journal of the Royal Meteorological Society*, *118*(507), 819–850.

Moncrieff, M. W. (2010). The multiscale organization of moist convection and the intersection of weather and climate. why does climate vary? *Geophysical Monograph Series, No. 189, American Geophysical Union*, 3–26. https://doi.org/doi:10.1029/2008GM000838

Moncrieff, M. W., & Klinker, E. (1997). Organized convective systems in the tropical western Pacific as a process in general circulation models: a TOGA COARE case-study. *Quarterly Journal of the Royal Meteorological Society*, *123*(540), 805–827.

Moorthi, S., & Suarez, M. J. (1992). Relaxed arakawa-schubert: A parameterization of moist convection for general circulation models. *Monthly Weather Review*, *120*, 978–1002.

Neelin, J. D., & Zeng, N. (2000). A quasi-equilibrium tropical circulation model-formulation. *Journal of the Atmospheric Sciences*, *57*(11), 1741–1766. https://doi.org/10.1175/1520-0469(2000)057<1741:AQETCM>2.0.CO;2

Pan, D. M., & Randall, D. D. A. (1998). A cumulus parameterization with a prognostic closure. *Quarterly Journal of the Royal Meteorological Society*, *124*(547), 949–981. https://doi.org/10.1002/qj.49712454714

Peters, K., Crueger, T., Jakob, C., & Möbis, B. (2017). Improved MJO-simulation in ECHAM6.3 by coupling a stochastic multicloud model to the convection scheme. *Journal of Advances in Modeling Earth Systems*, *9*, 193–219. https://doi.org/10.1002/2016MS000809

Peters, K., Jakob, C., Davies, L., Khouider, B., & Majda, A. (2013). Stochastic behavior of tropical convection in observations and a multicloud model. *Journal of the Atmospheric Sciences*, *70*, 3556–3575. https://doi.org/10.1175/JAS-D-13-031.1

Plant, R. S., & Craig, G. C. (2008). A stochastic parameterization for deep convection based on equilibrium statistics. *Journal of the Atmospheric Sciences*, *65*, 87–105.

Randall, D., Khairoutdinov, M., Arakawa, A., & Grabowski, W. (2003). Breaking the cloud parameterization deadlock. *Bulletin of the American Meteorological Society*, *84*(11), 1547–1564.

Randall, D., & Pan, D. M. (1993). Implementation of the Arakawa-Schubert cumulus parameterization with a prognostic closure. In *The representation of cumulus convection in numerical models* (K. A. Emanuel, & D. J. Raymond, Eds.), Meteorological Monographs. American Meteorological Society, Boston, MA.

Raymond, D. J., & Herman, M. J. (2011). Convective quasi-equilibrium reconsidered. *Journal of Advances in Modeling Earth Systems*, *3*, M08003. https://doi.org/10.1029/2011MS000079

Slingo, J. M., Sperber, K. R., Boyle, J. S., Ceron, J. P., Dix, M., Dugas, B., & Renno, N. (1996). Intraseasonal oscillation in 15 atmospheric general circulation models: Results from an AMIP diagnostic subproject. *Climate*, *12*, 325–357.

Stensrud, D. J. (2007). *Parametrization schemes: Keys to understanding numerical weather prediction models*. Cambridge: Cambridge University Press.

Sun, Y., Yi, L., Zhong, Z., & Ha, Y. (2014). Performance of a new convective parameterization scheme on model convergence in simulations of a tropical cyclone at grey-zone resolutions. *Journal of the Atmospheric Sciences*, *71*(6), 2078–2088. https://doi.org/10.1175/JAS-D-13-0285.1

Tiedtke, M. (1993). Representation of clouds in large-scale models. *Monthly Weather Review*, *121*(11), 3040–3061.

Waite, M., & Khouider, B. (2010). The deepening of tropical convection by congestus preconditioning. *Journal of the Atmospheric Sciences*, *67*, 2601–2615.

Wu, C. M., Stevens, B., & Arakawa, A. (2009). What controls the transition from shallow to deep convection? *Journal of the Atmospheric Sciences*, *66*, 1793–1806. https://doi.org/10.1175/2008JAS2945.1

Zhang, G. J., & McFarlane, N. A. (1995). Sensitivity of climate simulations to the parameterization of cumulus convection in the Canadian Climate Center general circulation model. *Atmos. Ocean*, *33*(3), 407–446.